

# Search for massive protostellar candidates in the southern hemisphere: I. Association with dense gas <sup>\*</sup>

F. Fontani<sup>1</sup>, M.T. Beltrán<sup>2</sup>, J. Brand<sup>3</sup>, R. Cesaroni<sup>2</sup>, L. Testi<sup>2</sup>, S. Molinari<sup>4</sup>, and C.M. Walmsley<sup>2</sup>

<sup>1</sup> Dipartimento di Astronomia e Fisica dello spazio, Largo E. Fermi 2, I-50125 Firenze, Italy

<sup>2</sup> INAF, Osservatorio Astrofisico di Arcetri, Largo E. Fermi 5, I-50125 Firenze, Italy

<sup>3</sup> Istituto di Radioastronomia, CNR, Via Gobetti 101, I-40129 Bologna, Italy

<sup>4</sup> IFSI, CNR, Via Fosso del Cavaliere, I-00133 Roma, Italy

Received date; accepted date

**Abstract.** We have observed two rotational transitions of both CS and C<sup>17</sup>O, and the 1.2 mm continuum emission towards a sample of 130 high-mass protostellar candidates with  $\delta < -30^\circ$ . This work represents the first step of the extension to the southern hemisphere of a project started more than a decade ago aimed at the identification of massive protostellar candidates. Following the same approach adopted for sources with  $\delta \geq -30^\circ$ , we have selected from the IRAS Point Source Catalogue 429 sources which potentially are compact molecular clouds on the basis of their IR colours. The sample has then been divided into two groups according to the colour indices [25–12] and [60–12]: the 298 sources with [25–12]  $\geq 0.57$  and [60–12]  $\geq 1.30$  have been called *High* sources, the remaining 131 have been called *Low* sources. In this paper, we check the association with dense gas and dust in 130 *Low* sources. We have obtained a detection rate of  $\sim 85\%$  in CS, demonstrating a tight association of the sources with dense molecular clumps. Among the sources detected in CS,  $\sim 76\%$  have also been detected in C<sup>17</sup>O and  $\sim 93\%$  in the 1.2 mm continuum. Millimeter-continuum maps show the presence of clumps with diameters in the range 0.2 – 2 pc and masses from a few  $M_\odot$  to  $10^5 M_\odot$ ; H<sub>2</sub> volume densities computed from CS line ratios lie between  $\sim 10^{4.5}$  and  $10^{5.5} \text{ cm}^{-3}$ . The bolometric luminosities of the sources, derived from IRAS data, are in the range  $10^3 - 10^6 L_\odot$ , consistent with embedded high-mass objects. Based on our results and those found in the literature for other samples of high-mass young stellar objects, we conclude that our sources are massive objects in a very early evolutionary stage, probably prior to the formation of an HII region. We propose a scenario in which *High* and *Low* sources are both made of a massive clump hosting a high-mass protostellar candidate and a nearby stellar cluster. The difference might be due to the fact that the 12  $\mu\text{m}$  IRAS flux, the best discriminant between the two groups, is dominated by the emission from the cluster in *Lows* and from the massive protostellar object in *Highs*.

**Key words.** Stars: formation – Radio lines: ISM – ISM: molecules, continuum

## 1. Introduction

Recently, an ever growing effort has been devoted to investigating the early evolutionary stages of massive stars ( $M \geq 8M_\odot$ ). In particular, attention has gradually shifted from the study of newly formed ZAMS stars to objects in an earlier evolutionary stage, prior to the formation of an HII region, deriving their luminosity from the release of gravitational energy: these objects are named *protostars*. The observational approach to searching for high-mass protostars was first formulated by Habing & Israel (1979): likely candidates must be associated with dense

circumstellar environments, not be associated with HII regions, and they should have high luminosities.

Following these criteria, with the aim of identifying massive protostellar candidates (with  $\delta \geq -30^\circ$ ), Palla et al. (1991) selected a sample of 260 sources from the IRAS Point Source Catalogue (IRAS-PSC) with 60  $\mu\text{m}$  flux greater than 100 Jy and colours satisfying the criteria established by Richards et al. (1987) for compact molecular cores. This sample was then divided into two groups according to their [25–12] and [60–12] colours: the *High* sources, which have [25–12]  $\geq 0.57$  and [60–12]  $\geq 1.30$  characteristic of association with UC HII regions (Wood & Churchwell 1989), and the *Low* sources, with complementary colours. Palla et al. found a lower association rate with H<sub>2</sub>O masers for the *Low* sources, and interpreted this as an indication of relative youth. In order to confirm this

Send offprint requests to: F. Fontani, e-mail: fontani@arcetri.astro.it

<sup>\*</sup> Based on results collected at the European Southern Observatory (ESO), La Silla, Chile.

result, and to better understand the nature of *High* and *Low* sources, the whole sample has been studied in various tracers, including molecular lines and continuum emission, from centimeter to near-infrared wavelengths (Molinari et al. 1996, 1998a, 2000, 2002; Brand et al. 2001; Zhang et al. 2001). The main findings of these studies are the following:

- *High* and *Low* sources have luminosities typical of intermediate- or high-mass objects ( $L \geq 10^3 L_\odot$ );
- a relatively large fraction of *High* sources is associated with UC HII regions (57%, Molinari et al. 1998a);
- the *Low* group contains a considerable fraction ( $\sim 76\%$ ) of likely precursors of stars with mass  $M > 10 M_\odot$ .

Furthermore, Molinari et al. (1998b) and more recently Fontani et al. (2004a, 2004b) have studied in detail, at low and high angular resolution, three sources belonging to the *Low* group which have been proposed as protostellar candidates: IRAS 23385+6053, IRAS 21307+5049 and IRAS 22172+5549. In all three cases, they have detected a compact ( $\sim 0.03 - 0.04$  pc), dense ( $\sim 10^7 \text{cm}^{-3}$ ) and massive ( $\sim 50 - 300 M_\odot$ ) molecular envelope, likely hosting an intermediate- to high-mass YSO in the protostellar phase.

The results obtained for sources with  $\delta \geq -30^\circ$  suggested an extension to sources with  $\delta < -30^\circ$  following the same approach, in order to complete this study. With this motivation, we have applied the selection criteria of Palla et al. (1991) to sources of the IRAS-PSC with  $\delta < -30^\circ$ , finding 298 *High* and 131 *Low* sources. It is worth noting that the samples selected by us likely contain a higher contamination of HII regions than those selected by Palla et al. (1991), because surveys of HII regions south of  $\delta < -30^\circ$  are much less numerous than those with  $\delta \geq -30^\circ$ .

When identifying massive protostellar candidates, the first step is to establish an association with dense molecular clumps. Dense gas is traced by warm dust emission from a massive core at millimeter and sub-millimeter wavelengths, and by millimeter rotational and inversion transitions of various molecular species, such as CS,  $\text{NH}_3$  and  $\text{C}^{17}\text{O}$ . In this paper we present observations obtained with the SEST-15m telescope of rotational transitions of CS and  $\text{C}^{17}\text{O}$ , and of the 1.2 mm continuum emission towards almost all (130 out of 131) sources belonging to the *Low* subsample.

All sources belonging to the *High* subsample have already been observed in the CS (2–1) line by Bronfman et al. (1996), who performed a complete survey in this line towards IRAS sources with [25–12] and [60–12] colours characteristic of UC HII regions with the SEST and the Onsala telescope.

Also, an alternative sample of high-mass protostellar candidates has been selected from the IRAS-PSC by Sridharan et al. (2002). They used selection criteria similar to those of Palla et al. (1991), with the important difference that they ruled out all *Low* sources, and therefore their sample is basically made of *High* sources. Then,

Beuther et al. (2002a) observed the molecular environment associated with these sources in some CS lines and 1.2 mm continuum. Therefore, their results, as well as those of Bronfman et al. (1996), are of great interest for the present paper, and will be used in the following for the sake of comparison to our findings. Hereafter, the sample selected by Sridharan et al. (2002) and observed in various tracers by Beuther et al. (2002a) will be called “Sridharan/Beuther sample”. All the sources detected in the CS (2–1) line by Bronfman et al. (1996) have been observed by Faundez et al. (2004) in the 1.2 mm continuum. However, we have not used their results in this paper because their work was published after our paper was submitted. They will be discussed in a forthcoming paper (Beltran et al., in prep.) entirely devoted to the observations of the millimeter continuum (see Sect. 3.3).

Sect. 2 describes the observations, and Sect. 3 presents the results. In Sect. 4 we derive the physical properties of the molecular clumps, which we discuss in Sect. 5. The conclusions are summarized in Sect. 6.

## 2. Observations

### 2.1. Molecular lines

Single-pointing observations of CS and  $\text{C}^{17}\text{O}$  were obtained with the SEST (Swedish-ESO Submillimetre Telescope) 15-m telescope at ESO-La Silla, Chile. In Table 1 we give the molecular transitions observed (Col. 1), the line rest frequencies (Col. 2), the telescope half-power beam width (HPBW, Col. 3), and the channel spacing (Col. 4) and total bandwidth (Col. 5) of the spectrometer used.

All observations were carried out towards the positions of the IRAS sources given in Table 3. We observed using dual beam switching with a  $11'37''$  throw. The data were calibrated with the chopper wheel technique (see Kutner & Ulich 1981). Pointing was checked every 1–2 hours on SiO masers at 7 mm. The pointing accuracy is estimated to be  $\sim 3''$ .

#### 2.1.1. CS

Observations of the CS (2–1), (3–2) and (5–4) lines were performed from May 23 to 25, 2001, and from May 6 to 11, 2002. We observed the (2–1), (3–2) and (5–4) lines respectively in 130, 128 and 3 out of 131 sources of the initial sample. The antenna temperature,  $T_A^*$  and the main beam brightness temperature  $T_{\text{MB}}$  are related as:  $T_{\text{MB}} = T_A^*/\eta_{\text{MB}}$ , with  $\eta_{\text{MB}} = 0.73, 0.66$  and  $0.50$  for CS (2–1), (3–2) and (5–4) respectively.

We simultaneously observed the (2–1) and (3–2) lines during the first observing run, and the (2–1) and (5–4) lines during the second observing run, using two Acousto-Optic Spectrometers: one with low spectral resolution and large bandwidth, and a second with higher spectral resolution and smaller bandwidth (see Table 1). Since the  $v_{\text{LSR}}$  was unknown for most sources we tuned the receivers to

**Table 1.** Observed transitions

molecular transition	frequency (GHz)	HPBW (")	$\Delta v^\dagger$ (km s <sup>-1</sup> )	Bandwidth <sup>†</sup> (km s <sup>-1</sup> )
CS (2–1)	97.980	51	0.13/2.12	130/3053
CS (3–2)	146.969	34	0.087/1.43	87/2059
CS (5–4)	244.935	21	0.052/0.86	52/1238
C <sup>17</sup> O (1–0)	112.359	45	0.11/1.85	110/2664
C <sup>17</sup> O (2–1)	224.714	22	0.057/0.93	57/1342

<sup>†</sup> the two values refer to the two spectrometers used.

the  $v_{\text{LSR}}$  of the tangent point for the source galactic longitude (see Table 3). The values of  $v_{\text{LSR}}$  used during the first and the second observing runs are listed in Cols. 4 and 5, respectively. The integration time ranged from 3 to 4.5 minutes. For some lines detected at the edge of the bandwidth in the first scan we integrated the minimum possible time to get a low S/N detection of the CS (2–1) line in low resolution; after having determined the  $v_{\text{LSR}}$  of the line, we then re-centered the high resolution backend and made another measurement.

For 5 sources (13558–6159, 15262–5541, 16170–5053, 16402–4943, 16581–4212) observed during the first run we obtained bad quality spectra. We thus repeated the observations in the second run.

### 2.1.2. C<sup>17</sup>O

C<sup>17</sup>O (1–0) and (2–1) lines were observed in the period from May 6 to 11, 2002. For sources previously detected in CS we have used the LSR velocity of these lines to center the backends. We have also observed 8 objects not detected in CS. For these, we used the same velocity adopted for the CS observations, computed as described in Sect. 2.1.1. We observed the (1–0) and (2–1) transitions simultaneously using the 3 and 1.3 mm receivers. As for the CS lines,  $T_{\text{MB}}$  and  $T_A^*$  are related as  $T_{\text{MB}} = T_A^*/\eta_{\text{MB}}$ , with  $\eta_{\text{MB}} = 0.70$  and 0.50 for the C<sup>17</sup>O(1–0) and (2–1) lines, respectively.

### 2.1.3. C<sup>17</sup>O fitting procedure

The C<sup>17</sup>O (1–0) and (2–1) rotational transitions have hyperfine structure (see e.g. Frerking & Langer 1981). To take this into account, we fitted the lines using METHOD HFS of the CLASS program, which is part of the GAG software developed at the IRAM and the Observatoire de Grenoble. This fits the lines assuming that all components have equal excitation temperatures, that the line separations are fixed at the laboratory values, and that the line widths are identical. This method also gives an estimate of the total optical depth of the lines based on the intensity ratio of the different hyperfine components.

## 2.2. Continuum

The 1.2 mm continuum observations were carried out with the 37-channel bolometer array SIMBA (SEST Imaging Bolometer Array) at the SEST, on July 16–20, 2002 and July 9–13, 2003.

Maps were obtained towards all sources detected in CS, with the exception of 10555–5949, and towards 12 sources undetected in CS. Around all IRAS sources, we mapped a region of size 900'' × 400'' (azimuth × elevation), which was scanned at a rate of 80''/s. The total integration time per map was about 15 minutes, and the typical noise level in the maps is 25–40 mJy/beam. Atmospheric opacity was determined from skydips, which were taken every 2 hours, and values at the zenith ranged between 0.21 and 0.50 (in 2002) and 0.13 and 0.30 (2003). The data were calibrated using observations of Uranus, made once or twice per day; the conversion factor ranged between 58 and 75 mJy/count in 2002, and between 50 and 69 in 2003. The pointing of the SEST was determined to be accurate within a few arcsec, by observing a strong continuum source every 2 hours. The HPBW is  $\sim 24''$ .

All data were reduced with the program MOPSI, written by R. Zylka (Grenoble), and according to the instructions given in the SIMBA Observers Handbook<sup>1</sup>, (2003).

## 3. Observational results

The observed sources are listed in Table 3. Column 1 gives the IRAS name, and the equatorial (J2000) coordinates of the IRAS source are listed in Cols. 2 and 3, respectively. In Cols. 4 and 5 we list the center velocities used for the CS observations during the first and the second run, respectively, chosen as explained in Sect. 2.1.1. In Cols. 6 to 8 we present the following information: detection (Y) or non-detection (N) in CS, C<sup>17</sup>O and 1.2 mm continuum, respectively (N.O. means “not observed”). For the millimeter continuum, we have considered as detected those sources which show emission above the 3 $\sigma$  level in the maps. In Col. 9 we give the angular separation,  $\Delta$ , between the IRAS source and the peak position of the millimeter continuum. For sources with multiple peaks (see Sect. 3.3),  $\Delta$  represents the separation between the IRAS position and the nearest peak.

<sup>1</sup> <http://puppis.ls.eso.org/staff/simba/manual/simba/index.htm>.

**Table 2.** Number of sources detected (Y), not detected (N) or not observed (N.O.) in C<sup>17</sup>O and 1.2 mm continuum among the 111 sources detected in CS.

	Y	N	N.O.
C <sup>17</sup> O	84	26	1
1.2 mm	101	8	2

### 3.1. CS lines

We observed 130 out of 131 sources of the initial sample, and detected CS emission in 111 of them, with a detection rate of  $\sim 85\%$ . This indicates a tight association of the sample with dense gas, as partially expected on the basis of our experience with sources in the northern hemisphere. In 14 sources, we have detected only the CS (2–1) transition, while in one source, 10555–5949, only the (3–2) line was detected. Only 3 sources were observed in CS (5–4), but none were detected. One can compare this result with that found by Bronfman et al. (1996) obtained with the SEST and the Onsala Telescope in their less sensitive survey toward *High* sources (see Sect. 1): they found a detection rate of  $\sim 80\%$  in the sources observed with the SEST. Adopting the same detection limit as Bronfman et al. (1996) ( $3\sigma \simeq 0.3$  K in main beam brightness temperature  $T_{\text{MB}}$ , which corresponds to  $\sim 6\sigma$  in our observations) we obtain a comparable detection rate of  $\sim 70\%$ . This shows that both *High* and *Low* sources with  $\delta < -30^\circ$  are similarly associated with dense gas.

In Table 4 we list the CS line parameters obtained from the high resolution spectra. Almost all observed lines are well fitted by Gaussians, and the parameters have been calculated from these fits, except where specified otherwise (see discussion below). The integrated intensities,  $\int T_{\text{MB}} dv$ , of the CS (2–1) and (3–2) lines are given in Cols. 2 and 5, respectively; the line peak velocities,  $v_{\text{LSR}}$ , are listed in Cols. 3 and 6, and Cols. 4 and 7 list the line widths at half maximum, FWHM. In Cols. 2 and 5 we also give the  $3\sigma$  level, in K km s<sup>−1</sup>, of the spectra for non-detected sources, obtained assuming an average value of FWHM=2.5 km s<sup>−1</sup>.

Several spectra show multiple velocity components (16187–4932, 16254–4844, 16344–4605, 16363–4645, 16535–4300, 17036–4033, 17225–3426, 17256–3631, 17285–3346, 17355–3241). For these sources, we have performed, where possible, Gaussian fits to all components (the corresponding Gaussian parameters are listed in Table 4). The two components detected in 16535–4300 have also been detected in the C<sup>17</sup>O lines, whereas for 16363–4645 none of them were detected in C<sup>17</sup>O. For all other sources with multiple components, only one component has also been detected in C<sup>17</sup>O. In Sect. 4, where we will derive the physical properties of the clumps, we will refer to the CS component which has also been revealed in C<sup>17</sup>O; for 16363–4645 and 16535–4300 we have chosen the strongest one.

There are cases also in which the line profiles are asymmetric or deviate significantly from a Gaussian shape. In some spectra the lines have two blended peaks (e.g. 10123–5727, 17040–3959 and 17377–3109). This could be due to the superposition of separate velocity components, or to self-absorption. Also, a few lines present broad wings (e.g. 13438–6203, 15579–5303, 16218–4931, and 16204–4916). Incidentally, we note that 15579–5303 and 16204–4916 have FWHM very much higher than all other lines ( $\sim 10$ – $11$  km s<sup>−1</sup>). For these lines, the parameters listed in Table 4 have been derived from moment integrals over the velocity intervals indicated in parentheses in Cols. 3 and 7.

### 3.2. C<sup>17</sup>O lines

We observed the C<sup>17</sup>O (1–0) and (2–1) lines towards all of the 111 sources detected in CS, and towards 8 sources not detected in CS. Emission was detected in 84 sources, all of them previously detected in CS (see Table 2): the C<sup>17</sup>O detection rate is thus  $\sim 76\%$  for sources detected in CS, and  $\sim 71\%$  for all observed sources. In Table 5 we give the line parameters obtained from the high resolution spectra: in Cols. 3, 4, 5 and 6 we list integrated intensity ( $\int T_{\text{MB}} dv$ ), peak velocity ( $v_{\text{LSR}}$ ), FWHM and opacity ( $\tau_{10}$ ) of the C<sup>17</sup>O (1–0) line, respectively. Cols. 8, 9, 10 and 11 show the same parameters for the C<sup>17</sup>O (2–1) line. The integrated intensities have been computed from integrals over the velocity ranges given in Cols. 2 and 7 of Table 5, while for the other parameters we have adopted the fitting procedure described in Sect. 2.1.3.

In several spectra the different hyperfine components are fairly well-resolved. Two examples are shown in Fig. 1, where we have also indicated the position of the hyperfine components. Only one source, 16535–4300, presents a secondary fainter velocity component as in the corresponding CS spectra. The optical depths show that the C<sup>17</sup>O (1–0) and (2–1) lines are optically thin in almost all detected sources. Therefore, in Sect. 4.1.2 we will assume optically thin conditions when computing kinetic temperatures and column densities of the molecule.

### 3.3. Millimeter continuum

We mapped 124 sources in the 1.2 mm continuum, among which 109 out of the 111 sources detected in CS, and a further 15 sources not detected in CS. Since the present paper is focused on the molecular emission, hereafter we will discuss only the maps of the sources detected in CS. The analysis of the 1.2 mm continuum maps of all observed sources will be available in a forthcoming paper (Beltran et al., in prep.) completely devoted to this purpose. In that work, we will also compare our data with those of Faundez et al. (2004), who observed the 1.2 mm continuum emission towards a sample of *High* sources.

The observations show the presence of dusty clumps in 101 out of 109 sources previously detected in CS (see

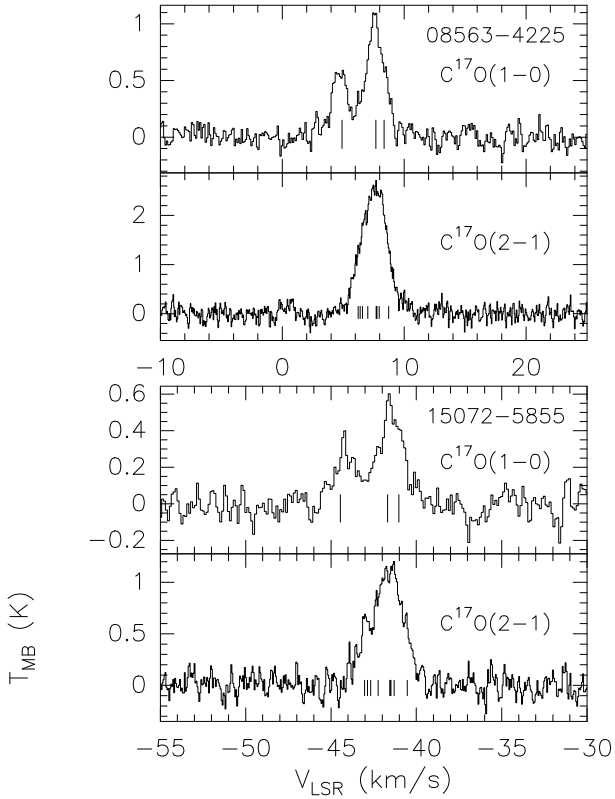


**Fig. 1.** Spectra of the  $C^{17}O$  (1–0) and (2–1) lines obtained towards 08563–4225 (top panels) and 15072–5855 (bottom panels). Vertical lines under the spectra indicate the hyperfine components.

Table 2), which translates into a detection rate of  $\sim 93\%$ . Morphologically, the maps show a large variety of features and structures. In several cases we detected an isolated clump, but only a small fraction of the clumps show a simple spherical symmetry (e.g. 17040–3959). Most of them have an elongated shape (e.g. 15557–5337), secondary faint peaks (e.g. 16535–4300) or a core-halo structure (e.g. 13481–6124). Additionally, the majority of the maps shows multiple clumps. One can distinguish between sources in which the clumps are separable (i.e. with the contours at half of the maximum well separated), and sources in which they are superimposed and not separable. In Fig. 2 we show an example of an isolated spherical clump, 17040–3959, and two examples of “clumpy” sources: in 10123–5727 the clumps are separable, while in 17225–3426 they are not.

As already said, a detailed analysis of these maps will be provided in a forthcoming paper. For the present discussion, we concentrate only on the continuum source associated with the line emission. Some physical parameters of the clumps, derived from the molecular line data in Sect. 4, require an estimate of the source angular diameter. Since we have not made maps in the molecular lines, this estimate has been obtained from the continuum maps, making the assumption that the millimeter continuum and the molecular lines trace the same region. Although some authors have shown that in clumps associated with high-

mass YSOs dust and molecular line emission may have different distribution (e.g. Fontani et al. 2004b), typically the angular diameters of their emitting regions are comparable. Thus, the assumption that the millimeter continuum and the molecular lines trace the same region is a reasonable approximation.

The lines were observed towards the position of the IRAS source; we have thus searched for the continuum source which is closest to the IRAS position. For sources with multiple clumps we have assumed that the IRAS source is associated with a particular continuum clump if the IRAS source lies within the clump’s  $3\sigma$  contour level. For sources in which none of the clumps includes the IRAS position, we have not assigned any “continuum source”.

Finally, several sources require a comment:

- 08477–4359: the IRAS position is between three faint peaks. In Table 3,  $\Delta$  is related to the nearest of these peaks.
- 14131–6126 and 14395–5941: we have identified a single clump, but the observed contour at half maximum is comparable to the HPBW. They are hence to be considered point-like sources;
- 16106–5048 and 16573–4214: have a filamentary structure similar to 17225–3426 (Fig. 2), in which we could not identify a clump coincident with the IRAS source;
- 15038–5828, 16153–5016, 16254–4844, 16403–4614, 16417–4445, 16428–4109, 17156–3607: show  $C^{17}O$  emission but no continuum emission. However, the  $C^{17}O$  lines are faint, and in several of these sources the non-detection of the millimeter continuum may be a “distance” effect. We will discuss this point in Sect. 4.2.3.

## 4. Derivation of the physical parameters

The main physical properties of the sources are presented in three tables: the parameters that do not depend on the source distance are listed in Table 6; in Table 7 we give distances, source linear diameters and luminosities, and in Table 8 we list the mass estimates. We now outline the methods used to derive each parameter, and present the results obtained.

### 4.1. Distance-independent parameters

The physical parameters which do not depend on the source distance are listed in Table 6: the angular diameter of the clumps (Col. 2), the 1.2 mm continuum flux densities (Col. 3), the kinetic temperature, the  $C^{17}O$  column density and the  $H_2$  total column density of the gas derived from the  $C^{17}O$  lines (Col. 4, 5 and 6, respectively) and the  $H_2$  volume density obtained from the CS data (Col. 7).

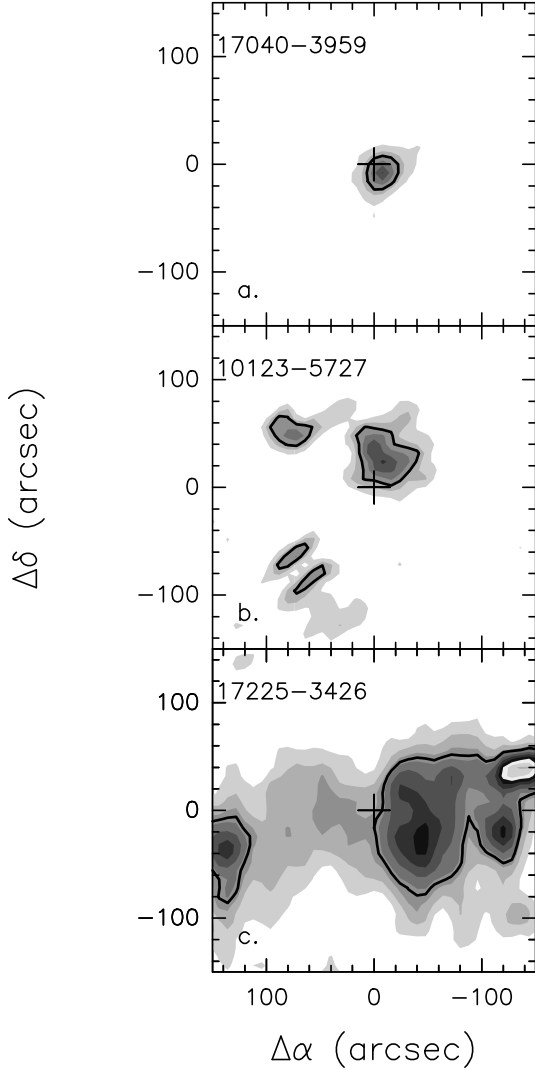


**Fig. 2.** Examples of various morphologies of the 1.2 mm continuum emission. **a:** 1.2 mm continuum map of 17040–3959. Contour levels range from 0.09 ( $\sim 3\sigma$ ) to 0.54 by 0.09 Jy beam $^{-1}$ . The cross indicates the position of the IRAS source. The solid line corresponds to the FWHM. **b:** same as **a** for 10123–5727. Contour levels range from 0.1 ( $\sim 3\sigma$ ) to 0.7 by 0.1 Jy beam $^{-1}$ . **c:** same as **a** for 17225–3426. Contour levels range from 0.07 ( $\sim 3\sigma$ ) to 1.07 by 0.1 Jy beam $^{-1}$ .

#### 4.1.1. Angular diameters

The angular diameters ( $\theta$ ) of the clumps identified in the 1.2 mm continuum maps (see Sect. 3.3) have been computed assuming the sources are Gaussian, and deconvolving the observed contour at half maximum with a Gaussian beam of  $24''$ . No angular diameter has been attributed to those sources for which the IRAS position does not lie within the  $3\sigma$  contour of any of the clumps identified in the maps. Moreover, we could not compute the angular diameters of 14131–6126 and 14395–5941, because they are not resolved (see Sect. 3.3). The diam-

eters range from  $\sim 10''$  to  $\sim 70''$ , and are distributed around  $\sim 35''$  (see Fig. 3 (a)).

In Fig. 3 (b) we plot the distribution of the quantity  $\Delta/\theta$ , where  $\Delta$  is the angular separation between the IRAS position and the millimeter continuum peak, listed in Table 3.  $\sim 80\%$  of the sources have  $0 \leq \Delta/\theta \leq 1$ , implying that the large majority of the identified clumps are indeed associated with the corresponding IRAS source. The maximum nominal uncertainty in the IRAS position is  $\sim 16''$ . To estimate the effect of this error on the quantity  $\Delta/\theta$ , we have considered the most pessimistic possibility by computing the distribution of the ratio  $(\Delta + 16)/\theta$ : we find that the number of sources with  $0 \leq \Delta/\theta \leq 1$  reduces to  $\sim 50\%$ . However, it is very unlikely that all the IRAS positions are affected by the maximum error. An "average" of  $8''$  is more plausible. Therefore, we have derived the distribution of  $(\Delta + 8)/\theta$ : in this case the fraction of sources with  $0 \leq \Delta/\theta \leq 1$  is  $\sim 70\%$ , which is very close to that found if we neglect the position uncertainty. Therefore, we believe that the uncertainty in the IRAS position do not significantly affect the distribution of  $\Delta/\theta$ .

Continuum flux densities,  $F_\nu$  (Col. 3 of Table 6), are obtained by integrating the maps over polygons circumscribing the identified clumps. For isolated clumps, this polygon corresponds to the  $3\sigma$  contour level; for multiple clumps, we have determined the polygon "by eye", trying to cut out contributions of secondary sources close to the main clump.

#### 4.1.2. Rotation temperature and $H_2$ column density from $C^{17}O$ lines

Cols. 4 and 5 of Table 6 list the rotation temperatures,  $T_{\text{rot}}$ , and  $C^{17}O$  column densities,  $N_{C^{17}O}$ , of the clumps derived from the  $C^{17}O$  data. By means of the angular diameters in Col. 2 we have corrected  $T_{\text{MB}}$  for the beam filling factor, thus obtaining the source-averaged brightness temperatures for the  $C^{17}O$  (1–0) and (2–1) lines. The rotation temperature and  $C^{17}O$  total column density were computed from the line ratios assuming LTE conditions and optically thin lines (see e.g. Hofner et al. 2000).

We find rotation temperatures distributed around  $\sim 8 - 10$  K, with the exception of 17256–3631, for which we obtain  $T_{\text{rot}} \sim 45$  K (see Fig. 3 (c)). We have also computed the  $H_2$  total column densities from  $N_{C^{17}O}$ , assuming a mean  $C^{17}O$  abundance relative to  $H_2$   $X_{C^{17}O} = N_{C^{17}O}/N_{H_2} \sim 3.9 \times 10^{-8}$  (Wilson & Rood 1994). They are found to be in the range  $\sim 10^{22} - 10^{24} \text{ cm}^{-2}$ . The values of  $N_{H_2}$  are of the same order as those found by Hofner et al. (2000) in their sample of UC HII regions, whereas those of  $T_{\text{rot}}$  are more than  $\sim 2$  times lower. We will discuss this result in Sect 5.1.

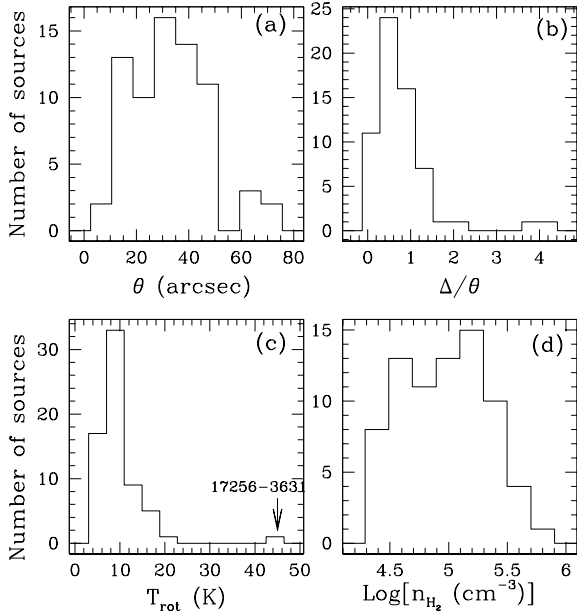


**Fig. 3.** Histograms of some distance-independent parameters. (a) angular diameters based on the SIMBA 1.2 mm continuum maps (HPBW  $\simeq 21''$ ). (b) ratio between angular separation between the IRAS position and the position of the millimeter peak ( $\Delta$ ) and the source angular diameter ( $\theta$ ). (c) rotation temperatures derived from C<sup>17</sup>O line ratios. (d) H<sub>2</sub> volume densities derived from CS line ratios.

#### 4.1.3. H<sub>2</sub> volume density from CS lines

We have used the LVG code of Cesaroni et al. (1991), with the collisional rates from Turner et al. (1992), to derive H<sub>2</sub> volume densities,  $n_{\text{H}_2}$ , from the CS lines. The LVG code computes the ratio between the brightness temperature,  $T_{\text{B}}$ , of the CS (2–1) and (3–2) transitions, as a function of the kinetic temperature,  $T_{\text{k}}$ , the H<sub>2</sub> volume density, the CS average abundance, and the velocity gradient,  $dv/dr$ . By comparing our data with the prediction of the models, and assuming that  $T_{\text{kin}} \sim T_{\text{rot}}$  from C<sup>17</sup>O, we can thus derive an estimate of the H<sub>2</sub> volume density.

We have first calculated the brightness temperature,  $T_{\text{b}}$ , of the lines from the measured  $T_{\text{MB}}$  according to the relation  $T_{\text{b}} = T_{\text{MB}}(1 + (\theta_{\text{MB}}/\theta)^2)$  (where  $\theta_{\text{MB}}$  is the Telescope HPBW and  $\theta$  is the source size), and computed the corresponding line ratio. Then, assuming a mean CS abundance of  $10^{-8}$  (Irvine et al. 1987), a velocity gradient of  $10 \text{ km s}^{-1} \text{ parsec}^{-1}$  (which is the mean value of the ratio between the linewidths and the clump diameters), and the temperature obtained from C<sup>17</sup>O (Sect. 4.1.2), we used the LVG code to estimate the value of  $n_{\text{H}_2}$  that could reproduce the ratio  $T_{\text{B}}[\text{CS}(2-1)]/T_{\text{B}}[\text{CS}(3-2)]$ . The same computation was repeated using the dust temperature,  $T_{\text{d}}$ , which will be derived in Sect. 4.2.2. For sources for which we could not derive the C<sup>17</sup>O temperature we have used a representative temperature  $T_{\text{rot}} = 10 \text{ K}$  (see

Fig. 3c). The values listed in Table 6 are the geometric mean of these two density estimates. The ratio between the two estimates is on average a factor of 3. We obtain  $n_{\text{H}_2} \sim 10^{4.5} - 10^{5.5} \text{ cm}^{-3}$ , as shown in Fig. 3 (d).

#### 4.2. Kinematic distances and distance-dependent parameters

Kinematic distances,  $d$ , are listed in Col. 2 of Table 7. They have been estimated from the CS line velocity using the rotation curve of Brand & Blitz (1993). The method is valid for distances from the galactic center between 2 and 25 kpc. We could not assign any distance to four sources (15371–5458, 17230–3531, 17410–3019 and 17425–3017), because the corresponding distance estimates were out of this interval.

For sources inside the solar circle, two solutions for the kinematic distance (*near* and *far*) are possible. In a few cases, this ambiguity can be solved: for sources that would be more than 150 pc from the galactic plane (i.e. twice the scale height of the molecular disk), the near distance was adopted. For one source (17040–3959), the near distance implies a value of the dust mass (see Sect. 4.2.3) which is very unlikely ( $\sim 0.02 M_{\odot}$ ), and hence the far distance was assumed, even though it is at 80 pc from the galactic plane. For all other sources we could not solve the distance ambiguity, and hence in Table 7 we give both values.

The physical parameters which depend on the source distance are listed in two tables: Table 7 gives the clump linear diameters, luminosities and dust temperatures (Col. 3, 4 and 5, respectively); Table 8 lists the masses estimated from dust emission (Col. 2), the virial masses (Col. 3), and the masses derived from the C<sup>17</sup>O and CS emission (Cols. 4 and 5, respectively). For sources with distance ambiguity, near and far estimates are listed in each column of both tables.

##### 4.2.1. Linear diameters and luminosities

The linear sizes have been computed from the angular diameters listed in Table 6, and are between  $\sim 0.1$  and  $\sim 2$  pc, typical of clumps hosting young high-mass objects (see e.g. Kurtz et al. 2000). The luminosities were calculated by integrating the IRAS flux densities. The contribution from longer wavelengths was taken into account by extrapolating according to a black-body function that peaks at  $100 \mu\text{m}$  and has the same flux as the source at that wavelength. The distribution of the luminosities for sources without distance ambiguity is shown in Fig. 4 (a): we find luminosities in the range  $\sim 10^3 - 10^5 L_{\odot}$ . For sources with distance ambiguity, in several cases the *far* estimate is also of order  $10^6 L_{\odot}$ . This confirms that the embedded sources are indeed intermediate- or high-mass objects.

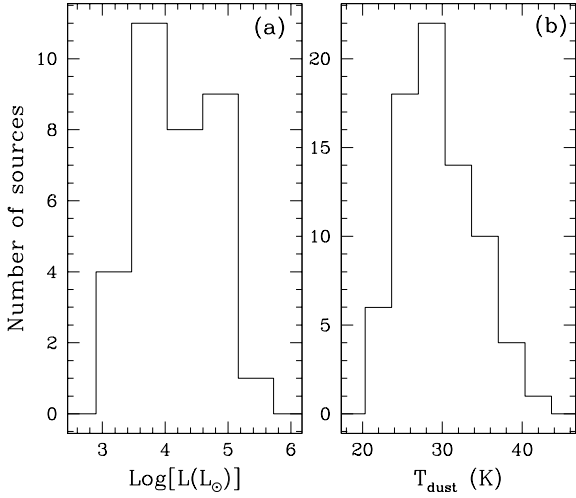


**Fig. 4.** (a): histogram of the luminosities for sources without distance ambiguity. (b): histogram of the dust temperature of the clumps, derived from grey-body fits to the SEDs.

#### 4.2.2. Dust temperatures

By fitting grey-bodies to the 1.2 mm continuum flux densities and the 60 and 100  $\mu\text{m}$  IRAS Point Source Catalog data, we have derived best-fit dust temperatures,  $T_d$ .

We find values of  $T_d$  distributed around  $\sim 30$  K (see Fig. 4 (b)), significantly higher ( $\sim$  a factor 3–4) than the rotation temperatures  $T_{\text{rot}}$  estimated from  $\text{C}^{17}\text{O}$  lines (Sect. 4.1.2). This difference is likely due to the fact that IRAS detects the emission of warm dust inside the innermost part of the clumps, whereas the  $\text{C}^{17}\text{O}$  (1–0) and (2–1) lines trace the more extended and colder envelope, because of the low excitation of the  $J = 0, 1, 2$  levels ( $\leq 16$  K).

As previously said, the values of  $T_d$  have been obtained by fitting only the millimeter point and the 60 and 100  $\mu\text{m}$  IRAS points of the SED (an example of a grey-body fit is shown in Fig. 5). In fact, in almost all observed sources the SED shows a shape that cannot be fitted with a single grey-body, but rather two grey-bodies: a “cold” one which fits the mm data and the IRAS 60 and 100  $\mu\text{m}$  points, and a “hot” one, which fits the 12 and 25  $\mu\text{m}$  data. Various authors (see e.g. Sridharan et al. 2002) have indeed shown that flux densities measured in different bands of the IRAS Catalogue do not necessarily arise from the same region. Furthermore, Molinari et al. (1998b) and Fontani et al. (2004a, 2004b) have recently demonstrated that in three *Low* sources of the sample selected by Palla et al. (1991) the 60 and 100  $\mu\text{m}$  emission arises from a compact core likely hosting a massive protostar, while the emission at 12 and 25  $\mu\text{m}$  is due to a cluster of more evolved IR sources surrounding the core. Therefore, the values of  $T_d$  listed in Table 7, derived by fitting only the points with  $\lambda \geq 60 \mu\text{m}$ , are representative of the cold dust component.

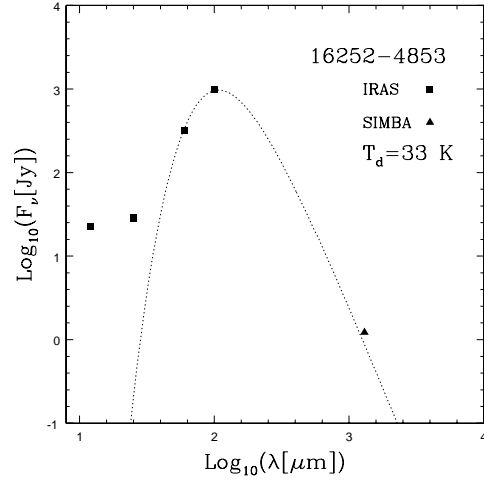


**Fig. 5.** SED of 16252–4853. Symbols have the meaning indicated in the top right-hand corner. The dotted line represents the best grey-body fit to points with  $\lambda \geq 60 \mu\text{m}$ , obtained for dust temperature of 33 K and dust opacity index  $\beta = 2$ .

In the fits we have assumed a dust opacity  $\kappa_\nu = \kappa_{230\text{GHz}}(\nu/\text{GHz})^\beta$ , where  $\kappa_{230\text{GHz}} = 0.005 \text{ cm}^2\text{g}^{-1}$ , which implies a gas-to-dust ratio of 100 (Kramer et al. 1998). We have also assumed  $\beta = 2$  which is a typical value derived for dusty envelopes of massive (proto)stellar objects (Hunter 1997; Molinari et al. 2000).

We stress that this is a simplified approach, since these regions can be very complex (as demonstrated by various authors, see e.g. Fontani et al. 2004a, 2004b) and a proper modeling of the SED would require many more details (source geometry, contribution of very small dust grains and PAHs). However, this approach would require a substantial number of assumptions and would go beyond the scope of this paper.

Our values of  $T_d$  are similar to those of the *Low* sources studied by Molinari et al. (2000), who derived in the same way the temperature of the cold dust in their sources. A similar analysis has been made by Sridharan et al. (2002), but they fitted the SED with two grey-bodies. We stress that, even if our estimates of  $T_d$  have been derived from a single grey-body, fitting the SED with two grey-bodies does not significantly affect the parameters that one derives from a single grey-body fit, because the two components refer to well-separated parts of the spectrum: typically, the correction would be  $< 5\%$ . Hence, our dust temperatures can be compared to those obtained by Sridharan et al. (2002): they derive an average value for  $T_d$  of the “cold” grey-body of  $\sim 50$  K, which is  $\sim 1.6$  times larger than that derived in this work for our sources.

#### 4.2.3. Mass estimates

Clump masses have been estimated using 4 different methods:



- One can compute the total mass from the dust millimeter-continuum emission ( $M_{\text{cont}}$ ) assuming optically thin conditions and a constant gas-to-dust ratio. Clump masses from mm continuum have also been derived by Beuther et al. (2002a) for the *High* sources of the Sridharan/Beuther sample (see Sect. 1). In order to make a consistent comparison with the masses derived by those authors, we compute  $M_{\text{cont}}$  with the relation used by them (see their Sect. 3.2):

$$M_{\text{cont}}(M_{\odot}) = 1.3 \times 10^{-3} F_{\nu}(\text{Jy}) [d(\text{kpc})]^2 \left[ \exp\left(\frac{h\nu}{kT_d}\right) - 1 \right] \left(\frac{\nu}{2.4\text{THz}}\right)^{-3-\beta} \quad (1)$$

This relation has been derived adopting the same dust opacity as used in Sect. 4.2.2, which assumes a gas-to-dust ratio of 100. We have also used the same opacity index,  $\beta = 2$ .

- From the line FWHM and the clump linear diameters, we can estimate the virial mass,  $M_{\text{vir}}$ . Assuming that the source is spherical and homogeneous, and neglecting the contributions of magnetic field and surface pressure, the virial mass is given by:

$$M_{\text{vir}}(M_{\odot}) = 0.509 d(\text{kpc}) \theta(\text{arcsec}) \Delta v^2(\text{km/s}) \quad (2)$$

where  $d$  is the source distance (Table 7),  $\theta$  the source angular diameter (Table 6) and  $\Delta v$  is the FWHM of the CS (2–1) line (Table 4).

- From the  $\text{H}_2$  total column density derived from the  $\text{C}^{17}\text{O}$  lines (Sect. 4.1.2) we may deduce the gas mass according to the expression:

$$M_{\text{C}^{17}\text{O}} = \frac{\pi}{4} D^2 N_{\text{H}_2} m_{\text{H}_2} \quad (3)$$

where  $D$  is the source diameter in Table 7,  $m_{\text{H}_2}$  the mass of the  $\text{H}_2$  molecule, and  $N_{\text{H}_2}$  is the beam-averaged column density (Table 6).

- Assuming a spherical source, we can compute the gas mass from the CS lines,  $M_{\text{CS}}$ , using the  $\text{H}_2$  average volume density derived from LVG calculations (see Sect. 4.1.3) and the source diameters given in Table 7.

All mass estimates are listed in Table 8. We find clump masses ranging from a few tens  $M_{\odot}$  up to  $\sim 10^5 M_{\odot}$ . We will discuss the different mass estimates in Sect. 5.4.

In Sect. 3.3 we pointed out that a few sources have been detected in  $\text{C}^{17}\text{O}$  but not in the millimeter continuum, and that this can be due to a “distance effect”. We can now justify this statement. From Eq. (1) one can estimate the continuum flux expected for a clump with mass  $M$  located at the far distance, and compare this with the sensitivity of our maps, to check if the emission is not detected because the clump is too far away. Since we have no direct estimate for the clump masses of these sources, we have assumed a representative value of  $10^3 M_{\odot}$ : we infer that, at the far distances given in Table 7, for 16153–5016, 16254–4844 and 16417–4445 the expected fluxes are  $\sim 0.07$  Jy, while for 15038–5828 and 16403–4614 they are  $\sim 0.15$  and  $\sim 0.13$  Jy, respectively. These values are comparable to the  $3\sigma$  level in the

maps, which is  $\geq 0.07$  Jy beam $^{-1}$ . We hence conclude that the non detection of these sources in the continuum could be due to our sensitivity limit and the fact that they are located at the far distance.

## 5. Discussion

The most important result of this work is that a large fraction ( $\sim 85\%$ ) of the sample is associated with dense gas, as partially expected on the basis of the criteria applied to select our sources. In Sect. 1 we have stressed that this work is the extension to  $\delta < -30^\circ$  of the project started by Palla et al. (1991) in the northern hemisphere, aimed at the identification of precursors of UC HII regions through a comparative study of *High* and *Low* sources. For this reason, in the following we will compare the properties derived in Sects. 3 and 4 to those of other well known samples of high-mass protostellar candidates and massive YSOs with IRAS colours typical of *High* sources.

### 5.1. Rotation temperatures from $\text{C}^{17}\text{O}$

The rotation temperatures derived in Sect. 4.1.2 from  $\text{C}^{17}\text{O}$  are distributed around  $\sim 8 - 10$  K. Molinari et al. (1996) found a mean value of  $\sim 22$  K for their sources, without any significant difference between *High* and *Low* sources, and Sridharan et al. (2002) found an average value of 19 K in their sample of massive protostar candidates. Furthermore, Brand et al. (2001) measured the rotation temperature in clumps associated with 6 *Low* sources, finding temperatures from  $\sim 20$  K to  $\sim 50$  K. However, both Molinari et al. (1996) and Sridharan et al. (2002) used  $\text{NH}_3$  lines in deriving  $T_{\text{rot}}$ , while Brand et al. (1996) used  $\text{CH}_3\text{C}_2\text{H}$  lines, which probably trace a different region of the clumps.

Hofner et al. (2000) made a survey of  $\text{C}^{17}\text{O}$  towards UC HII regions. They observed the  $\text{C}^{17}\text{O}$  (1–0), (2–1) and (3–2) lines with the IRAM–30m and the KOSMA–3m telescopes. The authors found temperatures from 13 to 41 K, with a mean value of  $\sim 23$  K. This value is higher than that derived by us. However, it must be noted that the  $\text{C}^{17}\text{O}$  (3–2) transition likely arises from a more internal and hotter region than that traced by the (1–0) and (2–1) lines. To allow a consistent comparison we have derived the rotation temperature of the sources of the Hofner et al. (2000) sample using only the transitions observed by us, namely the  $\text{C}^{17}\text{O}$  (1–0) and (2–1) lines: we thus obtain temperatures of  $\sim 20$  K on average. This value is marginally lower than that obtained by Hofner et al. (2000), and still  $\sim 2$  times higher than ours.

A possible explanation of this is that our sources are on average less luminous than the UC HII regions observed by Hofner et al. (2000). In fact, in clumps where the gas is heated by an embedded (proto)star with luminosity  $L$ , the gas temperature at a distance  $r$  from the central (proto)star is expected to scale as (see e.g. Doty & Leung 1994)  $T \propto (L^{1/2}/r)^\alpha$ , where  $\alpha$  typically varies between 0.3 and 0.5. Assuming coupling between gas and

dust, which is plausible for densities of  $\sim 10^5 \text{cm}^{-3}$ , this holds also for the dust temperature. Therefore, sources with higher luminosities are expected to be hotter at the same distance from the central object. Another possible explanation could be the role of the different angular resolution of the observations: Hofner et al. (2000) observed the  $\text{C}^{17}\text{O}$  (1–0) and (2–1) lines with an angular resolution two times better than ours. Therefore, they were observing lines arising from a more internal, and probably hotter, region of the clumps. On the basis of our data, it is impossible to discriminate between the two hypothesis presented above.

## 5.2. Linewidths

### 5.2.1. Comparison with UC HII regions

In Fig. 6 we show the distributions of the linewidths ( $\Delta v$ ) of the CS and  $\text{C}^{17}\text{O}$  lines (top and bottom panels, respectively), measured in Sects. 3.1 and 3.2. For the CS lines  $\Delta v$  is on average  $\sim 2.7 \text{ km s}^{-1}$ , with no significant difference between the (2–1) and (3–2) transitions. Such a mean value is much lower than that measured by Cesaroni et al. (1991) towards a sample of UC HII regions: they found linewidths from  $\sim 3.5 \text{ km s}^{-1}$  to  $\sim 9 \text{ km s}^{-1}$ , with an average value of  $\sim 6 \text{ km s}^{-1}$  in both transitions. For the  $\text{C}^{17}\text{O}$  lines, the mean value observed by us is  $\Delta v \sim 2 \text{ km s}^{-1}$  (see bottom panel of Fig. 6),  $\sim 3$  times lower than that found by Hofner et al. (2000), from observations of UC HII regions.

A possible interpretation of these results is that the turbulence is much lower in our clumps than in those associated with UC HII regions. The turbulence in high-mass star forming regions is due to a variety of phenomena (e.g. powerful outflows, winds, infall), and is correlated to the activity of the embedded objects: less evolved objects are thought to be associated with more quiescent envelopes. Therefore, the narrower lines found in our sources suggest that the embedded objects do not contain already formed stars. This interpretation is also supported by the results of Brand et al. (2001), who came to the same conclusion for their sample of northern *Low* sources.

### 5.2.2. Comparison with *High* sources

In the top panel of Fig. 7 we plot the linewidth of the CS (2–1) line against the [25–12] colour, and compare our data with those of Bronfman et al (1996). In order to make a consistent comparison, we have plotted only sources that have  $\delta < -30^\circ$  (namely sources which have all been observed with the SEST), and that satisfy the criteria adopted by Palla et al. (1991) to identify compact molecular clouds: since all Bronfman sources have colour indices  $[25-12] \geq 0.57$  and  $[60-12] \geq 1.3$  (see Sect. 1), the subsample selected by us consists of *High* sources. Hereafter, this subsample (190 sources) will be called “Bronfman sample”. It is worth noting that we cannot take out the HII regions from this sample because of the lack of ex-

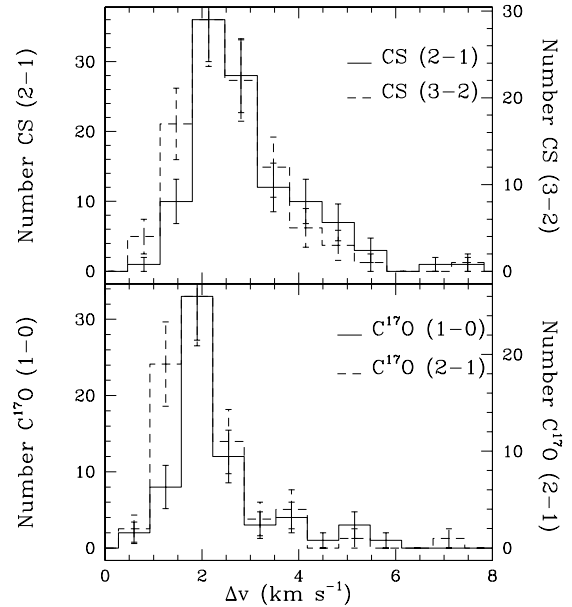


**Fig. 6.** Top panel: Histogram of the CS linewidths. Bottom panel: same as top panel for the  $\text{C}^{17}\text{O}$  linewidths.

tensive surveys of HII regions south of  $\delta = -30^\circ$ . The mean value of the data of the Bronfman sample is  $\sim 3.9 \text{ km s}^{-1}$  (median =  $3.9 \text{ km s}^{-1}$ ), with a standard deviation  $\sigma \simeq 1.5 \text{ km s}^{-1}$ , while for our sample we find a mean value of  $\sim 2.7 \text{ km s}^{-1}$  (median =  $2.6 \text{ km s}^{-1}$ ), with a standard deviation  $\sigma \sim 1.4 \text{ km s}^{-1}$ .

In the bottom panel, we show a comparison between our sample and the 69 *High* sources of the “Sridharan/Beuther sample” (see Sect. 1). The mean value that we derive for the Sridharan/Beuther sample is  $\sim 3.1 \text{ km s}^{-1}$  ( $\sigma \simeq 1.5 \text{ km s}^{-1}$ ), and the median is  $3.2 \text{ km s}^{-1}$ . From a purely statistical point of view, the linewidth distributions of the three samples are mutually consistent among them. However, from Fig. 7 one can notice that our sources and those of the Sridharan/Beuther sample have similar linewidths, whereas a small fraction (11 out of 190 sources) of the *High* sources of the Bronfman sample have linewidths larger than those measured by us and by Beuther et al. (2002a). More quantitatively, we find that approximately 10% of the sources in the Bronfman sample have  $\Delta v > 7 \text{ km s}^{-1}$ , while these percentages are  $< 5$  and  $< 1$  in the Sridharan/Beuther and in our sample, respectively. This may suggest that the *High* sources of the Bronfman sample have CS linewidths slightly different from those of the Sridharan/Beuther sample. However, as previously pointed out, the Bronfman sample also contains HII regions, which have been excluded from the Sridharan/Beuther sample. For this reason, we believe that the sources of the Bronfman sample which show larger linewidths are likely associated with HII regions. We conclude that *High* and *Low* sources not associated with HII regions have similar linewidths.

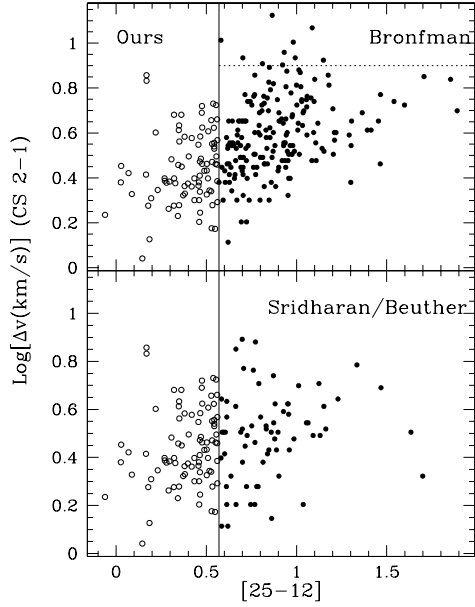


**Fig. 7.** Plot of the linewidths of the CS (2–1) transition against the [25–12] color index. Top panel: open circles represent *Low* sources observed by us; filled circles indicate potential UC HII regions observed by Bronfman et al. (1996), observed with the SEST, with  $\delta < -30^\circ$  and satisfying the criteria adopted by Palla et al. (1991): hence they are *High* sources. The dashed line indicates the maximum value of  $\Delta v$  measured for the sources of the Sridharan/Beuther sample. Bottom panel: same as Top panel for the sources observed by Sridharan et al. (2002).

### 5.2.3. Full width at zero intensity of the lines

The full width at “zero intensity” (FWZI) of a line provides information about the presence of non-Gaussian wings, and hence of an outflow. Since bipolar outflows are believed to be strictly related to the accretion process of forming stars of both low- and high-mass (see e.g. Beuther et al. 2002b), it is important to check the association of our sources with an outflow to better understand their nature. For this reason, we have measured the FWZI of the CS lines and compared them to the theoretical values expected from purely Gaussian lines. In the ideal case of a spectrum without noise, the wings of a Gaussian line asymptotically approach zero, and the FWZI tends to infinity. In the real spectra, the “zero intensity” depends on the noise level, and therefore the measured FWZI depends both on the FWHM and on the signal-to-noise ratio  $T_{\max}/\sigma$ , where  $T_{\max}$  is the line peak and  $\sigma$  is the rms noise in the spectrum. Taking as “zero intensity” the  $3\sigma$  level, one can demonstrate that the FWZI is related to the FWHM and the signal-to-noise ratio as follows:

$$\text{FWZI}_{\text{gauss}} = \frac{\text{FWHM}}{\sqrt{\ln 2}} \sqrt{\ln \left[ \frac{T_{\max}}{3\sigma} \right]}. \quad (4)$$

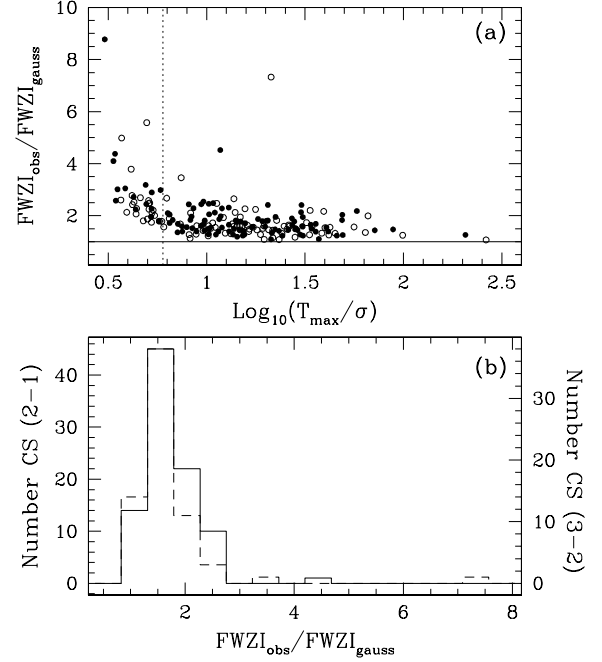


**Fig. 8.** (a) ratio between the observed full width at zero intensity ( $\text{FWZI}_{\text{obs}}$ ) and that expected for a line with Gaussian shape ( $\text{FWZI}_{\text{gauss}}$ ) from Eq. (4) for the CS (2–1) (filled circles) and (3–2) (empty circles) lines versus the signal-to-noise ratio ( $T_{\max}/\sigma$ ) of the spectra. Significant data are those with  $T_{\max}/\sigma > 6$  (to the right of the dotted line). (b) histograms of the quantity  $\text{FWZI}_{\text{obs}}/\text{FWZI}_{\text{gauss}}$  for both CS (2–1) (solid line) and (3–2) (dashed line) lines. Only sources with  $T_{\max}/\sigma > 6$  are considered here.

Deviations from this relationship are due to non-Gaussian wings, and may hence indicate the presence of an outflow.

In Fig. 8 (a) we plot the ratio between the observed FWZI ( $\text{FWZI}_{\text{obs}}$ ) and that expected from Eq. (4) as a function of the signal-to-noise ratio, both for the CS (2–1) and (3–2) lines. The values of  $\text{FWZI}_{\text{gauss}}$  have been computed from the FWHM listed in Table 4. The  $\text{FWZI}_{\text{obs}}$  are computed as the separation between the first channels on the right and left from the line peak with intensity lower than  $3\sigma$ . The significant data are those with line intensity at half maximum  $> 3\sigma$ , i.e. with  $T_{\max}/\sigma > 6$ . As expected, all observed lines have  $\text{FWZI}_{\text{obs}}/\text{FWZI}_{\text{gauss}} \geq 1$ . Fig. 8 (b) shows that the majority ( $\sim 70\%$ ) of our lines with  $T_{\max}/\sigma > 6$  has  $\text{FWZI}_{\text{obs}} \geq 1.5 \text{ FWZI}_{\text{gauss}}$ , suggesting the presence of outflows in many of our sources. The “most frequently occurring value” of  $\text{FWZI}_{\text{obs}}$  is  $\sim 6 \text{ km s}^{-1}$  for both the CS (2–1) and (3–2) lines, in good agreement with the values found by Brand et al. (2001) in a sample of 11 northern *Low* sources, in which they found an average value of  $5.9 \text{ km s}^{-1}$  for the CS (3–2) line.

### 5.3. Luminosities

#### 5.3.1. Comparison with *High* sources

In order to see if *High* and *Low* sources are associated with young stars of different masses, we verify if there is any significant difference in luminosity between our sources and those of the other samples of high-mass protostellar candidates. In Fig. 9 we compare the bolometric luminosities of our sources with those of the Bronfman sample (top panel), selected as explained in Sect. 5.2.2 and those of the Sridharan/Beuther sample (bottom panel). One can see that the sources in our sample and in that of Sridharan/Beuther have similar luminosities, mostly distributed between  $10^3$  and  $10^5 L_\odot$  (only two of them have  $L > 10^5 L_\odot$ ). This is consistent with the results of Palla et al. (1991), who noted that the luminosity distributions for the sources of the *High* and *Low* groups with  $\delta \geq -30^\circ$  are similar. On the other hand, in the Bronfman sample, which also includes HII regions,  $\sim 30\%$  of the sources have luminosities larger than  $10^5 L_\odot$ . Therefore, the sources with the highest bolometric luminosities are likely associated with HII regions (or equivalently with more massive stars), which are expected to be brighter at FIR wavelengths.

This explanation is further supported by the plots shown in Fig. 10, in which we present the distribution of the ratio between the radio-continuum flux, taken from the on-line NRAO VLA Sky Survey (NVSS) database<sup>2</sup>, and the IRAS integrated flux for both *High*s and *Lows* detected in the NVSS. The NVSS surveyed the sky north of  $\delta = -40^\circ$  at 1.4 GHz, with an angular resolution of  $\sim 45''$ . For further details about the NVSS data, see Condon et al. (1998).

In Fig. 10 (a) we have plotted all sources which satisfy the colour-colour criteria by Palla et al. (1991) belonging both to the northern and the southern sky. In Fig. 10 (b) we have plotted only those also associated with dense gas, i.e. detected in CS by Bronfman et al. (1996) (*High*s), and detected in CS in this work (*Lows*). Since the number of *Lows* detected by us and in the NVSS was low (only 6), we have included in the analysis the *Low* sources detected in  $\text{NH}_3$  by Molinari et al. (1996). The mean values of the NVSS-to-IRAS flux ratios are  $\sim 0.3$  (with standard deviation  $\sigma \sim 0.3$ ) for *High* sources, and  $\sim 0.2$  ( $\sigma \sim 0.2$ ) for *Low* sources, for the distributions of both Fig. 10 (a) and (b). Hence, *High*s and *Lows* have similar distributions of the NVSS-to-IRAS flux ratios. Although these values are very similar, the offset between the peaks of the distributions of *High*s and *Lows* in Figs. 10 (a) and (b) leads us to speculate that a fraction of the *High* sources has higher NVSS-to-IRAS flux ratios than the *Low* sources, suggesting that the former group might be more tightly associated with HII regions. It is also worth noting that the distributions shown in Figs. 10 (a) and (b) contain sources of *all* luminosities. In Fig. 10 (c) we have plotted

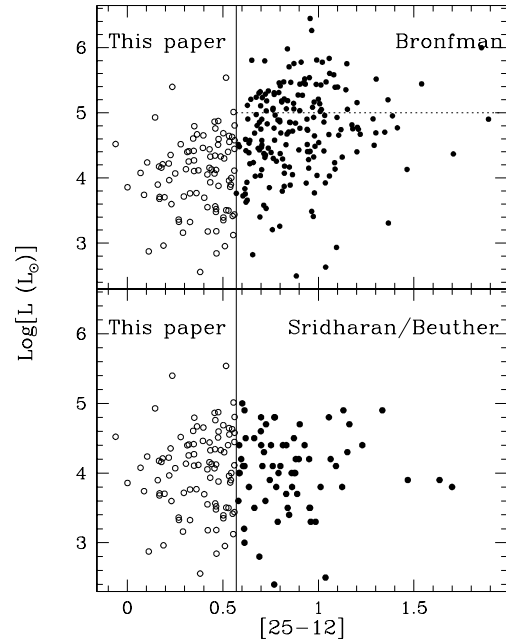


**Fig. 9.** Plot of the bolometric luminosity against the [25–12] color index. For sources with distance ambiguity the near value has been adopted. Top panel: open circles represent *Low* sources observed by us; filled circles indicate *High* sources observed by Bronfman et al. (1996), with  $\delta < -30^\circ$ . The dotted line indicates the maximum value of  $L_{\text{near}}$  found in the Sridharan/Beuther sample. Bottom panel: same as top panel for the sources of the Sridharan/Beuther sample.

only sources detected in dense gas with  $L < 10^5 L_\odot$ : this allows us to make a consistent comparison given the lack of sources with  $L > 10^5 L_\odot$  in the *Low* sample. Although the uncertainties are very large because the statistics are poor, especially for the *Low* sources, the NVSS-to-IRAS flux ratios are distributed similarly for the two groups: the mean values are  $\sim 0.24$  and  $\sim 0.19$  ( $\sigma \sim 0.2$ ) for *High*s and *Lows*, respectively. This means that the most luminous sources of the *High* group (which are excluded from this diagram) have the highest NVSS-to-IRAS fluxes, and thus are likely associated with evolved HII regions.

For this reason, we believe that the luminosities of *Low* and *High* sources *not associated* with HII regions are similar, and that the embedded high-mass objects likely have similar mass. This conclusion supports the results of the previous studies made by Molinari et al. (1998a, 2000) of the *High*s and *Lows* of the northern hemisphere.

#### 5.3.2. Mass-luminosity ratio and age of the sources

Another important parameter for establishing the age of a clump is the ratio between the mass of the clump and the corresponding luminosity,  $M/L$ . This is believed to decrease with time because during the star formation process more and more gas is converted into stars. Therefore, for

<sup>2</sup> The NVSS data are available at <http://www.cv.nrao.edu/nvss/>

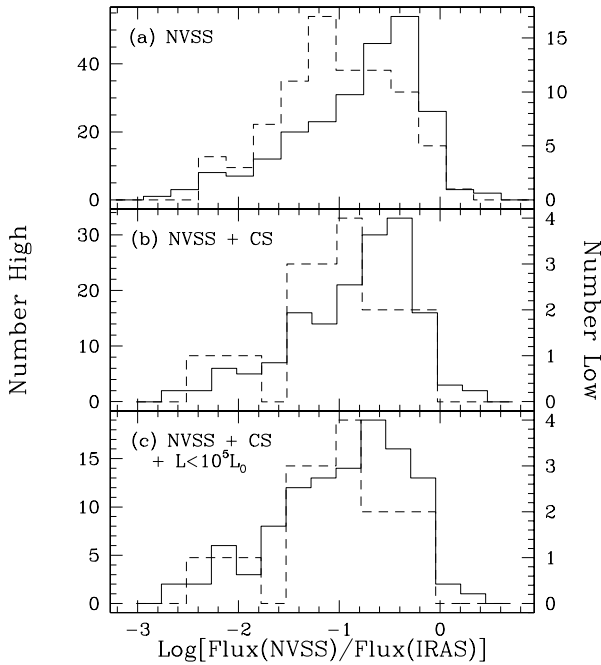


**Fig. 10.** Distribution of the ratio between the NVSS radio flux and the IRAS integrated flux for *High* (solid line) and *Low* (dashed line) sources. (a) Sources detected in NVSS; (b) Same as panel (a) for sources detected also in dense gas (CS for *High*s, CS or NH<sub>3</sub> for *Low*s; (c) Same as panel (b) for sources with luminosities lower than  $10^5 L_{\odot}$ .

clumps with *comparable masses*, the ratio  $M/L$  is an estimate of the degree of evolution of the embedded source. With this in mind, in Fig. 11, using the clump mass derived from dust emission,  $M_{\text{cont}}$ , we plot the histograms of the distance-independent quantity  $M/L$  for our *Low* sample, and the *High* sample of Sridharan/Beuther. No significant difference is seen between *High* and *Low* sources. Sridharan et al. (2002) have compared their sources to known UC HII regions, finding a lower  $M/L$  ratio in the latter. The clump masses of both samples were comparable, so that the authors interpreted this result as an indication of the relative youth of the sources of their sample. Since the clumps associated with our *Low* sources also have masses similar to those associated with the UC HII regions analysed by Sridharan et al. (2002) and the *High*s of the Sridharan/Beuther sample, the different  $M/L$  ratio can be interpreted the same way, namely that our sources, as well as those of the Sridharan/Beuther sample, are younger than UC HII regions.

In accretion-dominated models of the evolution of a massive protostar, one might expect to see correlation between the properties of the core from which the protostar is accreting and protostellar characteristics such as luminosity and outflow rate. From the recent models of Tan (2003) (see also McKee & Tan (2003)), one sees that there is a close connection between the accretion rate onto a protostar and the column density of the

clump in which it forms (or equivalently the surface density  $\Sigma = M_{\text{cont}}/\pi R^2$ ). Since the protostellar luminosity is partially due to accretion, it seems reasonable to examine the dependence of bolometric luminosity upon surface density for both our sample and the Sridharan/Beuther sample. The results (for sources without distance ambiguity) are shown in Fig. 12 where we also show theoretical predictions based on the results of Tan (2003) and Nakano et al. (1995). One sees that although there is a lot of scatter, there is a tendency for an increase in protostellar luminosity with clump column density. One also sees that in this diagram the *High* and *Low* samples behave essentially in the same fashion.

It is interesting moreover that there is rough agreement between the observations and predictions of the models for assumed protostar masses in the range  $5\text{--}20 M_{\odot}$  where we have assumed half of the final protostellar mass to have been accreted. We note also that there is a variety of assumptions involved in deriving the “theoretical curves” including the assumption that the luminosity is dominated by the most massive protostar of what presumably is an embedded cluster. Another uncertainty involves the protostellar radius. To make this point clear, we show results in Fig. 12 for two extreme assumptions concerning the protostellar radius: the value on the ZAMS and that derived according to the prescription of Nakano et al. (1995). We note that while the former appears to give better agreement with the data of Fig. 12, the latter is probably preferable both for theoretical reasons discussed by Nakano et al. and because of the fact that the predicted Lyman continuum luminosities are much lower with this assumption, consistent with the observation of little or no centimeter continuum emission. In this case however, the predicted dependence of luminosity upon  $\Sigma$  is completely flat because the protostellar radius becomes proportional to the accretion rate and we need other indicators (such as outflow) to test the hypothesis that we are observing accreting protostars.

#### 5.4. Mass comparison and stability of the clumps

The masses estimated from the 1.2 mm continuum, the CS and C<sup>17</sup>O lines are compared to those deduced from the virial equilibrium (see Table 8) in Figs. 13, ( $\sigma = 0.3$ ), in which we present histograms of the ratio between the virial mass and the mass estimated with the other methods. The average ratio between  $M_{\text{CS}}$  and  $M_{\text{vir}}$  is  $\sim 0.8$  ( $\sigma = 0.7$ ), and between  $M_{\text{C}^{17}\text{O}}$  and  $M_{\text{vir}}$  is  $\sim 0.5$  ( $\sigma = 0.8$ ). The only mass estimate to be significantly different from the others is the mass obtained from the 1.2 mm continuum, as demonstrated by Fig. 13: the mean ratio between  $M_{\text{cont}}$  and  $M_{\text{vir}}$  is  $\sim 3.3$ , with a standard deviation  $\sigma \sim 2.7$ .

However, it must be noted that the virial mass, the CS mass and the C<sup>17</sup>O mass have been obtained from the physical parameters deduced from the *lines* and the diameter of the *continuum* region: they are hence “hybrid” quantities, and thus prone to unpredictable uncertain-

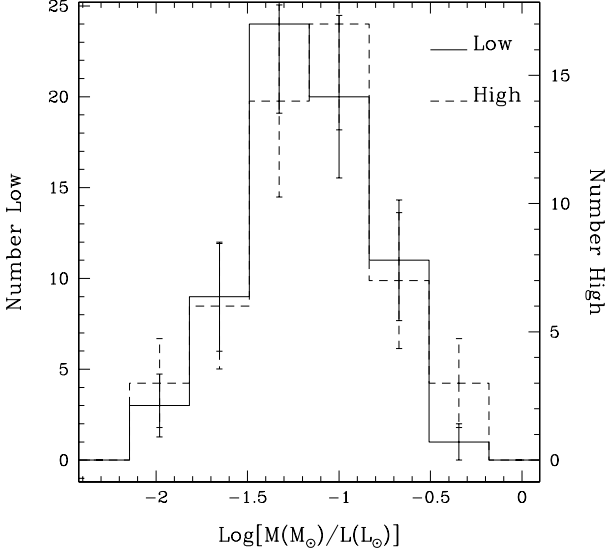


**Fig. 11.** Distribution of the distance-independent quantity  $M/L$ , where  $M$  is the clump mass derived from dust emission, for our *Low* sources (solid line) and the *High* sources of the Sridharan/Beuther sample (dashed line). For both distributions, the mean value is  $\sim 0.07 M_{\odot}/L_{\odot}$ .

ties. Furthermore,  $M_{\text{vir}}$  was calculated for homogeneous clumps: various authors (see e.g. Hatchell et al. 2000, Beuther et al. 2002a, Fontani et al. 2002) have shown that clumps associated with high-mass YSOs have density distributions described by a power-law of the type  $n \propto r^{-p}$ , with  $p$  typically ranging from  $\sim 1.5$  to  $\sim 2.5$ . Such density profiles can significantly affect the estimates of  $M_{\text{vir}}$  (see MacLaren 1988): for example, for  $p = 2$ ,  $M_{\text{vir}}$  becomes a factor  $\sim 1.6$  smaller. Thus, the ratio  $M/M_{\text{vir}}$  can also be affected by steep density profiles in the clumps.

A better estimate would require knowledge of the diameter of the line emitting region, which is not available. However, one can compare our results to those obtained by Brand et al. (2001), who mapped 11 *Low* sources with  $\delta \geq -30^\circ$  in various molecular lines, among which CS (3–2). From the CS (3–2) lines they found a gas-to-virial mass ratio lower than one, consistent with our result for  $M_{\text{CS}}/M_{\text{vir}}$  and  $M_{\text{C}^{17}\text{O}}/M_{\text{vir}}$ . Therefore, we can reasonably conclude that, within the uncertainties, our clumps could be virialized.

### 5.5. Where are the protostars?

The results discussed in Sects. 5.2 and 5.3 show that in several respects (linewidth distribution, luminosity distribution, mass-luminosity ratio, NVSS-to-IRAS flux ratio) the *Low* and *High* sources with luminosity  $L < 10^5 L_{\odot}$  are very similar. In particular, both samples seem to be associated with high-mass protostellar objects. One might be tempted to conclude therefore that the IRAS colours, on

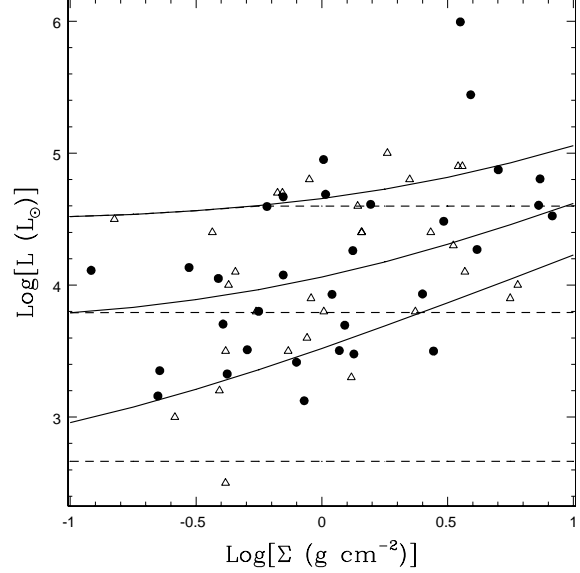


**Fig. 12.** Plot of the bolometric luminosity,  $L$ , of our sources and those of the Sridharan/Beuther sample versus the gas surface density derived from dust emission,  $\Sigma = M_{\text{cont}}/\pi R^2$ . Filled circles represent our *Low* sources; Open triangles correspond to the *High*s of the Sridharan/Beuther sample. The solid lines are theoretical curves for an accreting protostar (from top to bottom) with mass 20, 10 and  $5 M_{\odot}$ , assuming the ZAMS radius as protostellar radius. The dashed lines are the predictions obtained assuming the protostellar radius from Nakano et al. (1995).

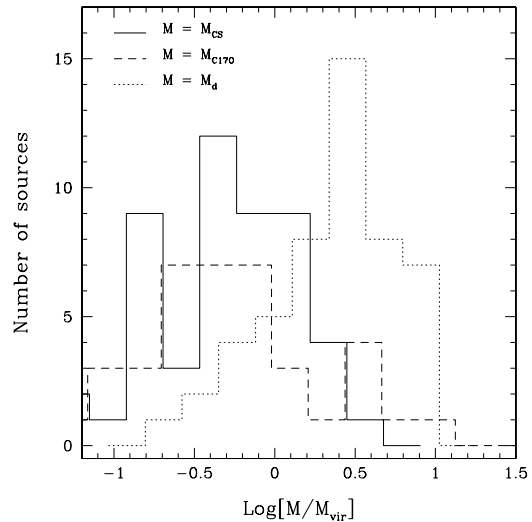


**Fig. 13.** Histograms of the ratio between the virial mass  $M_{\text{vir}}$  and the clump masses estimated with other methods: from CS ( $M_{\text{CS}}$ , solid line), from  $\text{C}^{17}\text{O}$  ( $M_{\text{C}^{17}\text{O}}$ , dashed line) and from dust emission ( $M_{\text{cont}}$ , dotted line).

which the distinction between *Highs* and *Lows* is based, are irrelevant for determining the evolutionary stage of these objects. At a first glance, this result seems to contradict the conclusions of previous studies of *Highs* and *Lows* with  $\delta \geq -30^\circ$  (Palla et al. 1991, Molinari et al. 1996, 1998a, 2000, Brand et al. 2001), namely that massive protostars are more likely to be found in the *Low* group. Let us try to shed light on this issue.

The distinction between the two groups is basically due to the different shape of the SED between 12 and 25  $\mu\text{m}$ . This is evident from Fig. 14, where we have plotted the average values of the IRAS fluxes for *High* and *Low* sources of the sample selected by Palla et al. (1991), normalised to the flux at 100  $\mu\text{m}$ ,  $F_{100}$ . Clearly, the average observed 12/100  $\mu\text{m}$  flux ratio is  $\sim 2$  times larger for *Low* sources than for *High* sources. The emission at this wavelength is due to hot dust; thus a crucial point concerning the difference between the two groups is understanding the origin of the hot dust.

Recently, Fontani et al. (2004a, 2004b) have shown that three *Low* sources of the initial sample are surrounded by a stellar cluster of more evolved stars. Given the large beam of the IRAS observations ( $\sim 30''$  at 12  $\mu\text{m}$ , which translates into  $\sim 0.15$  pc at 1 kpc), the IRAS measurements at 12  $\mu\text{m}$  are likely to be significantly affected by the emission of such a neighbouring cluster. We indeed concluded that, in these three sources, the mid-infrared continuum fluxes are dominated by the emission from the stellar cluster. Moreover, the presence of a stellar cluster in the surroundings of the molecular cores has also been established for a few *High* sources (e.g. IRAS 05385+3545, Porras et al. 2000 and IRAS 20126+4104, Cesaroni et al. 1997). Based upon these results and those of this paper, we suggest a scenario in which *both Highs* and *Lows* have a high-mass protostellar object embedded in a molecular core, and a stellar cluster located close to the core, but in the *Low* sources the flux at 12  $\mu\text{m}$  is dominated by the emission from the cluster, whereas the latter is less prominent towards *High* sources.

Note, however, that a nearby stellar cluster has been studied only in a few sources, and further observations at high angular resolution at near- and mid-infrared wavelengths are absolutely required to support the proposed scenario.

## 6. Conclusions

We have extended to the southern hemisphere the project started by Palla et al. (1991) in the northern sky aimed at identifying high-mass protostellar candidates. From the IRAS-PSC we have selected 131 *Low* and 298 *High* sources with  $\delta < -30^\circ$  using the same criteria as Palla et al. (1991). With the aim of testing whether the sources of the *Low* group are associated with dense gas, we have observed the CS (2–1) and (3–2) and  $\text{C}^{17}\text{O}$  (1–0) and (2–1) rotational transitions, and the 1.2 mm continuum emission towards all sources belonging to the *Low* group, since the *High* sources had already been observed in CS

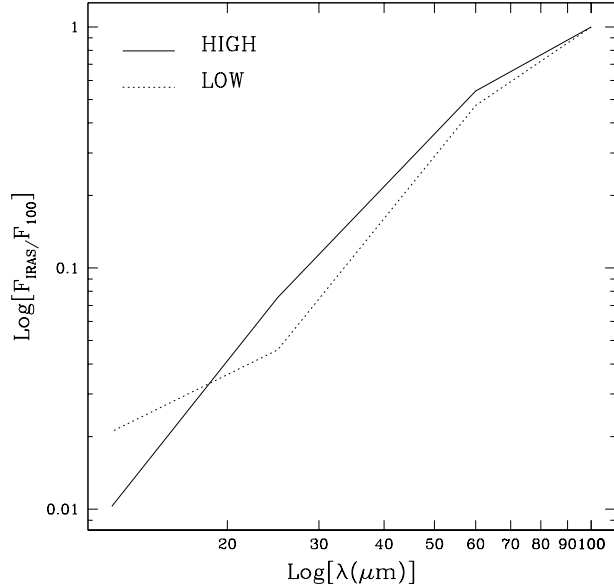


**Fig. 14.** Plot of the average IRAS fluxes (normalised for the flux at 100  $\mu\text{m}$ ,  $F_{100}$ ) for *High* (solid line) and *Low* (dotted line) sources.

(2–1) by Bronfman et al. (1996). The main findings obtained in this work are:

- The detection rate of  $\sim 85\%$  in CS demonstrates a tight association of the sources with dense gas. Among the sources detected in CS,  $\sim 76\%$  have also been detected in  $\text{C}^{17}\text{O}$  and  $\sim 93\%$  in 1.2 mm continuum.
- Continuum maps show the presence of clumps with diameters in the range 0.2 – 2 pc and masses from a few  $M_\odot$  to  $10^5 M_\odot$ ; clump kinetic temperatures derived from  $\text{C}^{17}\text{O}$  line ratios are mostly distributed in the range  $\sim 8 - 10$  K;  $\text{H}_2$  volume densities computed from CS line ratios lie between  $\sim 10^{4.5}$  and  $\sim 10^{5.5} \text{ cm}^{-3}$ .
- The bolometric luminosities of the sources, derived from IRAS data, are in the range  $10^3 - 10^6 L_\odot$ , consistent with embedded high-mass objects.

Comparing our results to those found in samples of high-mass YSOs with colours typical of *High* sources, we find that:

- The luminosities of our sources are comparable to those found by Sridharan et al. (2002) in their sample of high-mass YSOs. This suggests that both samples contain massive YSOs with comparable masses.
- The linewidths derived in this study are comparable to those observed in the sample by Sridharan et al. (2002), but significantly lower than those typically found in clumps associated with UC HII regions. Hence, our clumps are less turbulent than those associated with UC HII regions. This can be due to a lower degree of activity of the central objects.

- The distribution of the NVSS-to-IRAS flux ratios of *High* and *Low* sources of *all* luminosities shows that the *High* sources have higher NVSS-to-IRAS flux ratios. The same comparison obtained for sources with  $L < 10^5 L_\odot$  shows instead similar distributions for *High*s and *Low*s: this indicates that the brightest *High* sources are probably associated with more luminous stars and/or evolved HII regions.
- The mass-luminosity ratios found by us are similar to those of Sridharan et al. (2002) but lower than the ratio found for a sample of UC HII regions. Assuming that clumps of similar masses will form similar stellar clusters, this result further supports that our sources, as well as those of Sridharan et al. (2002), are younger than UC HII regions.

Our comparative study suggests that *High*s and *Low*s with  $L < 10^5 L_\odot$  are both associated with massive molecular clumps with similar physical parameters, indicating that the IRAS colours, on which the distinction between the two groups is based, are not indicative of the relative evolutionary stage. Based upon these results and those recently achieved by other authors, we propose that both samples are made of massive clumps hosting high-mass protostars, and nearby stellar clusters which are chiefly responsible for the observed 12  $\mu\text{m}$  IRAS flux in *Low* sources. Observations with high angular resolution in the near- and mid-infrared are absolutely required to confirm this scenario.

*Acknowledgements.* It is a pleasure to thank the ESO/SEST staff for their support during the observations. We thank Robert Zylka (IRAM Grenoble) for helping us with the SIMBA data reduction, and for his suggestions that improved the quality of the reduction scripts we used. We also thank the Referee, Dr. Gary Fuller, for his useful suggestions and comments.

## References

- Beuther, H., Schilke, P., Menten, K.M. et al. 2002, ApJ, 566, 945
- Beuther, H., Schilke, P., Sridharan, T.K. et al. 2002, A&A, 383, 892
- Brand, J. & Blitz, L. 1993, A&A, 275, 67
- Brand, J., Cesaroni, R., Palla, F., Molinari, S. 2001, A&A, 370, 230
- Bronfman, L., Nyman, L.-A., May, J. 1996, A&AS, 115, 81
- Cesaroni, R., Walmsley, C.M., Kompe, C., Churchwell, E. 1991, A&A, 252, 278
- Cesaroni, R., Felli, M., Testi, L., Walmsley, C.M., Olmi, L. 1997, A&A, 325, 725
- Condon, J.J., Cotton, W.J., Greisen, E.W. et al. 1998, AJ, 115, 1693
- Doty, S.D., Leung, C.M. 1994, ApJ, 4242, 729
- Faundez, S., Bronfman, L., Garay, G., Chini, R., Nyman, L.-A. et al. 2004, A&A, 426, 97
- Fontani, F., Cesaroni, R., Caselli, P., Olmi, L. 2002, A&A, 389, 603
- Fontani, F., Cesaroni, R., Testi, L., Walmsley, C.M., Molinari, S. et al. 2004a, A&A, 414, 299
- Fontani, F., Cesaroni, R., Testi, L., Molinari, S., Zhang, Q. et al. 2004b, A&A, 424, 179
- Frerking, M.A. & Langer, W.D. 1981, J. Chem. Phys., 74, 6990
- Habing, H.J., Israel, F.P. 1979, ARA&A, 17, 345
- Hatchell, J., Fuller, G., Millar, T., Thompson, M., MacDonald, G. 2000, A&A, 357, 637
- Hofner, P., Wyrowski, F., Walmsley, C.M., Churchwell, E. 2000, ApJ, 536, 393
- Hunter, T. 1997, Ph.D. thesis, Caltech
- Irvine, W.M., Goldsmith, P.F., Hjalmarson, H. 1987, Interstellar processes, ed. Hollenback D.J., Thronson H.A., 561
- Kramer, C., Alves, J., Lada, C. et al. 1998, A&A, 329, L33
- Kurtz, S., Cesaroni, R., Churchwell, E., Hofner, P., Walmsley, C.M. 2000, Protostars and Planets IV, ed. V. Mannings, A. Boss, & S. Russel (Tucson:Univ. of Arizona Press)
- Kutner, M.L. & Ulich, B.L. 1981, ApJ, 250, 341
- MacLaren, I., Richardson, K.M., Wolfendale, A.W. 1998, ApJ, 333, 821
- McKee, C.F. and Tan, J. 2003, ApJ, 585, 850
- Molinari, S., Brand, J., Cesaroni, R., Palla, F. 1996, A&A, 308, 573
- Molinari, S., Brand, J., Cesaroni, R., Palla, F., Palumbo G.G.C. 1998a, A&A, 336, 339
- Molinari, S., Testi, L., Brand, J., Cesaroni, R., Palla, F. 1998b, ApJ 505, L39
- Molinari, S., Brand, J., Cesaroni, R., Palla, F. 2000, A&A, 355, 617
- Molinari, S., Testi, L., Rodriguez, L.F., Zhang, Q. 2002, ApJ, 570, 758
- Nakano, T., Hasegawa, T., Norman, C. 1995, ApJ, 450, 183
- Palla, F., Brand, J., Cesaroni, R., Comoretto, G., Felli, M. 1991, A&A, 246, 249
- Plume, R., Jaffe, D.T., Evans II, N.J., et al. 1997, ApJ, 476, 730
- Porras, A., Cruz-Gonzales, I., Salas, L. 2000, A&A, 361, 660
- Richards, P.J., Little, L.T., Heaton, B.D., Toriseva, M. 1987, MNRAS, 228, 43
- Sridharan, T.K., Beuther, H., Schilke, P., Menten, K.M., Wyrowski, F. 2002, ApJ, 566, 931
- Tan, J. 2003 in "Galactic Star Formation across the Stellar Mass Spectrum", ed. J.M. De Buizer
- Turner, B.E., Chan, Kin-Wing, Green, S., Lubowich, D.A. 1992, ApJ 399, 114
- Wilson, T.L., Rood, R.T. 1994, ARA&A, 32, 191
- Wood, D.O.S., Churchwell, E. 1989, ApJS, 69, 831
- Wyrowski, F. 1997, Ph.D. thesis, Univ. of Cologne
- Zhang, Q., Hunter, T.R., Brand, J. et al. 2001, ApJL, 552, 167

## 7. tables



**Table 3.** Observed sources and detection summary. R.A.(J2000) and Dec.(J2000) represent the equatorial coordinates of the IRAS source.  $v_{\text{LSR}}$  is the velocity at which we centered the CS spectra during the two observing runs (see text). N.O. means that the source was not observed in that tracer.  $\Delta$  is the angular separation between the IRAS position and the nearest millimeter peak detected in the SIMBA maps.

IRAS name	R.A.(J2000)	Dec.(J2000)	$v_{\text{LSR}}$ (km s <sup>-1</sup> )		CS	C <sup>17</sup> O	1.2 mm	$\Delta$ ( $''$ )
			run I	run II				
08211–4158	08:22:52.3	–42:07:57	16.0	–	Y	Y	Y	10
08247–4223	08:26:27.6	–42:33:05	16.1	–	Y	N	Y	40
08477–4359	08:49:32.9	–44:10:47	70.6	–	Y	Y	Y	30
08488–4457	08:50:38.2	–45:08:18	62.1	–	N	N.O.	♠	–
08563–4225	08:58:12.5	–42:37:34	20.9	–	Y	Y	Y	15
09014–4736	09:03:09.8	–47:48:28	0.0	–	Y	N	Y	5
09026–4842	09:04:22.2	–48:54:21	0.0	–	Y	Y	Y	16
09131–4723	09:14:55.5	–47:36:13	0.0	–	Y	Y	Y	30
09166–4813	09:18:26.6	–48:26:26	0.0	–	Y	Y	Y	80
09209–5143	09:22:34.6	–51:56:23	0.0	–	Y	Y	Y	5
10088–5730	10:10:38.7	–57:45:32	18.8	–	N	N.O.	♠	–
10095–5843	10:11:15.8	–58:58:15	0.0	–	Y	Y	Y	15
10102–5706	10:12:03.7	–57:21:26	0.0	–	Y	N	N	–
10123–5727	10:14:08.8	–57:42:12	0.0	–	Y	Y	Y	30
10156–5804	10:17:26.8	–58:19:46	0.0	–	N	N	N	–
10277–5730	10:29:35.4	–57:45:34	0.0	–	Y	N	Y	25
10308–6122	10:32:39.8	–61:37:33	–7.3	–	Y	N	Y	10
10317–5936	10:33:38.1	–59:51:54	0.0	–	Y	N	Y	25
10439–5941	10:45:54.0	–59:57:03	0.0	–	Y	Y	Y	15
10521–6031	10:54:11.0	–60:47:30	0.0	–	Y	N	Y	25
10537–5930	10:55:49.0	–59:46:47	0.0	–	Y	N	Y	20
10545–6244	10:56:32.9	–63:00:34	0.0	–	Y	N	N	–
10548–5929	10:56:51.9	–59:45:14	0.0	–	Y	N	Y	15
10554–6237	10:57:25.0	–62:53:10	0.0	–	Y	Y	Y	10
10555–5949	10:57:37.5	–60:05:32	0.0	–	Y	N.O.	N.O.	–
10572–6018	10:59:19.3	–60:34:10	0.0	–	Y	N	Y	40
10575–5844	10:59:40.3	–59:01:05	0.0	–	N	N	N	–
10591–5934	11:01:15.8	–59:51:01	0.0	–	Y	N	Y	30
11265–6158	11:28:50.9	–62:15:01	0.0	–	Y	N	Y	15
11294–6257	11:31:46.5	–63:14:25	0.0	–	Y	N	Y	15
11380–6311	11:40:27.6	–63:27:56	0.0	–	Y	Y	Y	25
11396–6202	11:42:01.5	–62:19:24	0.0	–	Y	N	Y	60
11404–6215	11:42:48.0	–62:32:20	39.0	–	Y	Y	Y	40
11476–6435	11:50:08.0	–64:52:20	0.0	–	N	N.O.	♠	–

**Table 3.** Continued.

IRAS name	R.A.(J2000)	Dec.(J2000)	$v_{\text{LSR}}$ (km s <sup>-1</sup> )		CS	C <sup>17</sup> O	1.2 mm	$\Delta$ ( $''$ )
			run I	run II				
12102–6133	12:12:57.9	–61:50:17	0.0	–	Y	N	Y	50
12295–6224	12:32:22.7	–62:41:25	0.0	–	Y	Y	Y	15
12377–6237	12:40:42.4	–62:54:09	0.0	–	Y	N	Y	0
12434–6355	12:46:24.6	–64:11:26	0.0	–	N	N.O.	♠	–
13023–6213	13:05:30.7	–62:29:58	–10.0	–	Y	Y	Y	15
13039–6108	13:07:07.0	–61:24:47	–30.0	–	Y	Y	Y	22
13078–6247	13:11:05.1	–63:03:48	0.0	–	N	N.O.	♠	–
13106–6050	13:13:50.5	–61:06:44	0.0	–	Y	Y	Y	8
13333–6234	13:36:45.7	–62:49:36	–30.0	–	Y	Y	Y	16
13384–6152	13:41:53.3	–62:07:36	0.0	–	Y	Y	Y	10
13395–6153	13:42:59.5	–62:08:43	0.0	–	Y	Y	Y	16
13438–6203	13:47:21.9	–62:18:41	–30.0	–	Y	Y	Y	40
13481–6124	13:51:37.8	–61:39:08	0.0	–	Y	Y	Y	0
13558–6159	13:59:27.0	–62:13:40	–30.0	–45.0	N	N.O.	♠	–
13560–6133	13:59:35.3	–61:48:17	0.0	–	Y	Y	Y	40
14000–6104	14:03:36.6	–61:18:28	0.0	–	Y	Y	Y	0
14131–6126	14:16:48.6	–61:40:26	–30.0	–	Y	Y	Y	20
14166–6118	14:20:19.5	–61:31:53	–30.0	–	Y	Y	Y	0
14183–6050	14:22:02.8	–61:04:18	0.0	–	Y	N	Y	10
14198–6115	14:23:33.2	–61:28:53	0.0	–	N	N.O.	♠	–
14201–6044	14:23:54.2	–60:57:45	–30.0	–	Y	Y	Y	20
14395–5941	14:43:20.9	–59:53:54	0.0	–	Y	Y	Y	25
14412–5948	14:45:04.1	–60:01:14	0.0	–	N	N.O.	♠	–
14425–6023	14:46:23.5	–60:35:45	0.0	–	Y	Y	Y	15
14591–5843	15:02:58.8	–58:55:06	–40.0	–	Y	N	Y	40
15038–5828	15:07:43.8	–58:39:53	0.0	–	Y	Y	Y	100
15072–5855	15:11:07.9	–59:06:30	–20.0	–	Y	Y	Y	18
15100–5903	15:14:00.0	–59:15:09	–40.0	–	Y	Y	Y	36
15178–5641	15:21:45.4	–56:52:42	–30.0	–	Y	N	Y	15
15219–5658	15:25:48.7	–57:09:11	–20.0	–	Y	Y	Y	15
15239–5538	15:27:49.3	–55:48:42	–40.0	–	Y	N	Y	40
15246–5612	15:28:32.6	–56:23:00	–20.0	–	Y	Y	Y	15
15262–5541	15:30:05.5	–55:52:01	–20.0	–55.7	Y	Y	Y	40

**Table 3.** Continued.

IRAS name	R.A.(J2000)	Dec.(J2000)	$v_{\text{LSR}}$ (km s <sup>-1</sup> )		CS	C <sup>17</sup> O	1.2 mm	$\Delta$ ( $''$ )
			run I	run II				
15347–5518	15:38:36.0	–55:28:07	–40.0	–	Y	Y	Y	0
15371–5458	15:40:58.6	–55:08:20	30.0	–	Y	N	Y	0
15470–5419	15:50:55.2	–54:28:22	–20.0	–	Y	Y	Y	33
15506–5325	15:54:32.2	–53:33:53	–50.0	–	N	N.O.	♠	–
15519–5430	15:55:50.4	–54:38:58	–10.0	–	Y	Y	Y	34
15557–5337	15:59:38.2	–53:45:32	–40.0	–	Y	Y	Y	30
15571–5218	16:01:00.4	–52:27:13	–50.0	–	Y	N	N	–
15579–5303	16:01:46.6	–53:11:41	–20.0	–	Y	Y	Y	0
15579–5347	16:01:52.6	–53:56:21	–20.0	–	N.O.	N.O.	♠	–
15583–5314	16:02:10.1	–53:22:35	–50.0	–	Y	Y	Y	15
16061–5048	16:09:57.3	–50:56:45	–50.0	–	Y	Y	Y	25
16082–5031	16:12:03.2	–50:39:16	–32.4	–	Y	Y	Y	10
16093–5015	16:13:05.2	–50:23:05	–60.0	–	Y	Y	Y	40
16093–5128	16:13:09.2	–51:36:26	–50.0	–	Y	Y	Y	25
16106–5048	16:14:26.8	–50:56:12	–21.5	–	Y	Y	Y	?
16107–4956	16:14:29.4	–50:03:51	–60.0	–	Y	Y	Y	20
16148–5011	16:18:35.2	–50:18:53	–60.0	–	Y	Y	Y	0
16153–5016	16:19:07.0	–50:24:12	–23.4	–	Y	Y	Y	100
16170–5053	16:20:53.2	–51:00:14	–60.0	–54.0	Y	N	Y	50
16187–4932	16:22:29.3	–49:39:02	–60.0	–	Y	Y	Y	38
16194–4934	16:23:13.2	–49:40:59	–25.2	–	Y	Y	Y	35
16204–4916	16:24:12.3	–49:23:34	–60.0	–	Y	Y	Y	20
16204–4943	16:24:15.5	–49:50:05	–60.0	0.0	N	N.O.	♠	–
16218–4931	16:25:37.9	–49:38:20	–50.0	–	Y	Y	Y	0
16219–4848	16:25:39.4	–48:55:12	–60.0	–	Y	Y	N	–
16231–4819	16:26:49.1	–48:25:49	–60.0	–	Y	N	N.O.	–
16232–4917	16:27:02.0	–49:23:52	–50.0	–	Y	Y	Y	20
16252–4853	16:29:01.6	–48:59:48	–60.0	–	Y	Y	Y	16
16254–4844	16:29:09.0	–48:51:27	–60.0	–	Y	Y	Y	80
16344–4605	16:38:08.6	–46:11:10	–50.0	–	Y	Y	Y	15
16358–4614	16:39:29.4	–46:20:44	–60.0	–	N	N	N.O.	–

**Table 3.** Continued.

IRAS name	R.A.(J2000)	Dec.(J2000)	$v_{\text{LSR}}$ (km s <sup>-1</sup> )		CS	C <sup>17</sup> O	1.2 mm	$\Delta$ ( $''$ )
			run I	run II				
16363–4645	16:40:00.5	–46:51:32	–60.0	–	Y	Y	Y	25
16369–4810	16:40:38.2	–48:16:00	–60.0	–	Y	Y	Y	?
16403–4614	16:44:01.5	–46:20:27	–50.0	–	Y	Y	N	–
16404–4518	16:44:05.9	–45:23:53	–60.0	–	N	N	N.O.	–
16417–4445	16:45:19.9	–44:51:00	–60.0	–	Y	Y	N	–
16419–4602	16:45:37.9	–46:07:49	–	–60.0	Y	Y	Y	25
16428–4109	16:46:22.6	–41:14:58	–60.0	–	Y	Y	N	–
16464–4359	16:50:01.0	–44:05:03	–50.0	–	Y	Y	Y	10
16501–4314	16:53:41.1	–43:19:23	–50.0	–	Y	Y	Y	?
16535–4300	16:57:05.5	–43:05:20	–60.0	–	Y	Y	Y	20
16573–4214	17:00:54.3	–42:19:10	–	–25.0	Y	Y	Y	?
16581–4212	17:01:38.8	–42:17:05	–90.0	0.0	N	N.O.	♠	–
17033–4035	17:06:49.3	–40:39:51	–60.0	–	Y	Y	Y	30
17036–4033	17:07:08.9	–40:37:08	–60.0	–	Y	Y	Y	10
17040–3959	17:07:33.7	–40:03:04	0.0	–	Y	Y	Y	15
17082–4114	17:11:46.2	–41:18:03	–	–40.0	Y	Y	Y	40
17114–3804	17:14:52.2	–38:07:26	–30.0	–	N	N	N.O.	–
17140–3747	17:17:28.1	–37:51:06	–30.0	–	N	N	N	–
17141–3606	17:17:28.2	–36:09:38	0.0	–	Y	N	Y	30
17156–3607	17:19:01.2	–36:10:12	–30.0	–	Y	Y	N	–
17211–3537	17:24:28.5	–35:40:13	–20.0	–	Y	Y	Y	4
17218–3704	17:25:14.0	–37:07:29	–50.0	–	Y	Y	Y	25
17225–3426	17:25:50.3	–34:29:21	–30.0	–	Y	Y	Y	?
17230–3531	17:26:26.3	–35:33:35	–20.0	–	Y	Y	Y	5
17256–3631	17:29:01.1	–36:33:38	–20.0	–	Y	Y	Y	25
17285–3346	17:31:48.1	–33:48:23	0.0	–	Y	Y	Y	12
17338–3044	17:37:03.9	–30:46:17	0.0	–	Y	Y	Y	30
17355–3241	17:38:50.5	–32:43:35	0.0	–	Y	Y	Y	5
17368–3057	17:40:05.8	–30:58:51	0.0	–	N	N	N.O.	–
17377–3109	17:40:57.2	–31:11:00	0.0	–	Y	Y	Y	10
17410–3019	17:44:14.9	–30:20:42	0.0	–	Y	Y	Y	25
17419–3207	17:45:10.4	–32:08:48	0.0	–	N	N	N.O.	–
17425–3017	17:45:45.1	–30:18:51	0.0	–	Y	Y	Y	20

♠ the continuum maps will be available in a forthcoming paper (Beltran et al., in prep.)

**Table 4.** CS line parameters obtained from Gaussian fits( $\diamond$ ). Typical rms noise in the spectra is  $\sim 0.05$  K and 0.06 K for the (2–1) and (3–2) lines, respectively.

source	CS(2–1)			CS(3–2)		
	$\int T_{\text{MB}} dv$ (K km s $^{-1}$ )	$v_{\text{LSR}}$ (km s $^{-1}$ )	FWHM (km s $^{-1}$ )	$\int T_{\text{MB}} dv$ (K km s $^{-1}$ )	$v_{\text{LSR}}$ (km s $^{-1}$ )	FWHM (km s $^{-1}$ )
08211–4158	2.61(0.03)	10.80	1.76	1.99	10.93	1.59
08247–4223	0.42	8.04	1.5	0.38	7.81	1.9
08477–4359	2.27	8.47	2.97	1.82	8.15	2.76
08488–4457	$\leq 0.36$	–	–	$\leq 0.30$	–	–
08563–4225	9.22	7.66	3.78	9.51	7.67	3.54
09014–4736	0.39	3.26	2.14	$\leq 0.30$	–	–
09026–4842	2.65	5.15	1.83	2.06	5.26	1.68
09131–4723	3.74	4.03	2.43	2.72	4.03	2.62
09166–4813	0.82	6.28	1.9	0.29	6.47	1.19
09209–5143	0.97	36.85	1.89	$\leq 0.33$	–	–
10088–5730	$\leq 0.34$	–	–	$\leq 0.33$	–	–
10095–5843	3.62	–4.57	2.40	3.16	–4.38	1.98
10102–5706 $\blacklozenge$	0.48	–3.59(–7,0)	2.12	$\leq 0.33$	–	–
10123–5727 $\blacklozenge$	4.60	–4.03(–7,–1)	2.73	2.39	–3.87(–7,–1)	2.47
10156–5804	$\leq 0.25$	–	–	$\leq 0.25$	–	–
10277–5730	1.10	10.65	2.5	1.23	10.95	2.68
10308–6122	0.72	–6.65	2.32	0.52	–6.90	2.28
10317–5936	0.62	37.35	3.47	$\leq 0.33$	–	–
10439–5941	5.34	–14.57	2.42	4.33	–14.54	2.01
10521–6031	0.87	23.81	2.3	0.48	23.88	2.0
10537–5930	0.68	15.38	3.7	$\leq 0.33$	–	–
10545–6244	0.39	–11.62	1.9	0.31	–11.21	1.47
10548–5929	0.75	18.85	2.7	0.56	19.16	2.23
10554–6237	3.58	–16.78	2.18	2.61	–16.69	2.07
10555–5949	$\leq 0.31$	–	–	0.49	28.08	2.1
10572–6018	0.93	13.09	2.6	0.75	13.19	1.89
10575–5844	$\leq 0.33$	–	–	$\leq 0.33$	–	–
10591–5934	1.15	–25.92	2.1	0.59	–25.47	2.4
11265–6158	1.42	–23.27	1.96	1.12	–23.21	1.76
11294–6257	1.04	–26.13	2.0	$\leq 0.36$	–	–
11380–6311	4.06	–11.33	2.71	2.67	–11.09	2.70
11396–6202	0.62	41.07	2.38	$\leq 0.33$	–	–
11404–6215	1.77	38.86	2.9	1.78	39.07	2.75
11476–6435	$\leq 0.30$	–	–	$\leq 0.36$	–	–
12102–6133	0.54	–32.58	1.6	0.27	–32.41	0.9
12295–6224	3.51	–36.83	2.21	2.44	–36.48	2.11
12377–6237	0.44	22.0	2.8	$\leq 0.36$	–	–

Table 4. Continued.

source	CS(2–1)			CS(3–2)		
	$\int T_{\text{MB}} dv$ (K km s <sup>−1</sup> )	$v_{\text{LSR}}$ (km s <sup>−1</sup> )	FWHM (km s <sup>−1</sup> )	$\int T_{\text{MB}} dv$ (K km s <sup>−1</sup> )	$v_{\text{LSR}}$ (km s <sup>−1</sup> )	FWHM (km s <sup>−1</sup> )
12434–6355	≤ 0.36	—	—	≤ 0.33	—	—
13023–6213	3.22	−43.19	2.82	2.55	−42.99	2.46
13039–6108	1.65	−26.21	1.70	0.95	−26.15	1.39
13078–6247	≤ 0.33	—	—	≤ 0.33	—	—
13106–6050	3.42	−57.32	2.37	1.90	−57.42	2.24
13333–6234	8.66	−11.44	4.54	7.13	−11.14	3.73
13384–6152	2.75	−50.44	2.57	1.53	−50.36	2.04
13395–6153	18.04	−50.84	3.83	17.52	−50.75	3.69
13438–6203 <sup>♣</sup>	3.27	−51.27(−58, −46)	6.03	0.43	−51.10	2.1
13481–6124	8.12	−41.38	3.13	5.05	−40.98	2.68
13558–6159	≤ 0.35	—	—	≤ 0.36	—	—
13560–6133	3.38	−58.37	4.05	3.18	−58.56	3.44
14000–6104	3.53	−58.92	4.3	4.74	−58.95	4.24
14131–6126	0.77	−34.54	1.34	0.84	−34.42	1.44
14166–6118	1.63	−41.12	2.96	0.94	−41.05	2.67
14183–6050	0.60	−42.64	1.10	1.13	−42.65	1.43
14198–6115	≤ 0.36	—	—	≤ 0.36	—	—
14201–6044	0.94	−49.84	1.89	0.94	−49.65	1.93
14395–5941	1.53	−42.40	2.22	0.98	−42.25	3.17
14412–5948	≤ 0.38	—	—	≤ 0.36	—	—
14425–6023	5.97	−45.89	3.13	5.24	−45.74	3.19
14591–5843	1.14	−29.69	4.1	≤ 0.33	—	—
15038–5828	1.64	−67.14	3.65	≤ 0.35	—	—
15072–5855	4.73	−41.74	2.19	4.11	−41.65	2.23
15100–5903	1.79	−51.27	2.39	0.70	−50.91	2.77
15178–5641	0.90	−28.47	4.8	≤ 0.33	—	—
15219–5658	2.93	−15.99	4.0	2.99	−16.05	4.12
15239–5538	0.76	−46.79	2.5	0.41	−46.44	3.6
15246–5612	5.50	−65.44	3.06	3.57	−65.35	2.65
15262–5541	1.00	−54.15	2.9	0.17	−54.61	0.96
15347–5518	3.77	−61.54	3.04	2.59	−61.36	2.88
15371–5458	0.62	31.98	3.84	0.65	32.3	4.8
15470–5419	3.83	−61.73	4.9	3.11	−61.43	3.97
15506–5325	≤ 0.32	—	—	≤ 0.35	—	—
15519–5430	10.92	−36.53	2.87	8.34	−36.40	2.72
15557–5337	46.28	−47.12	4.21	56.82	−47.02	4.51
15571–5218 <sup>♣</sup>	1.40	−101.3(−107, −98)	5.36	0.70	−100.7(−107, −98)	4.84

Table 4. Continued.

source	CS(2–1)			CS(3–2)		
	$\int T_{\text{MB}} dv$ (K km s <sup>−1</sup> )	$v_{\text{LSR}}$ (km s <sup>−1</sup> )	FWHM (km s <sup>−1</sup> )	$\int T_{\text{MB}} dv$ (K km s <sup>−1</sup> )	$v_{\text{LSR}}$ (km s <sup>−1</sup> )	FWHM (km s <sup>−1</sup> )
15579–5303 <sup>♣</sup>	15.2	−49.8(−60,−34)	11.87	14.45	−49.25(−62,−34)	11.60
15583–5314	2.57	−77.58	2.44	1.08	−77.30	2.15
16061–5048	3.72	−51.81	2.88	1.71	−51.67	2.07
16082–5031	2.10	−41.00	2.31	1.51	−40.95	2.26
16093–5015	2.43	−42.93	2.04	1.28	−42.82	1.66
16093–5128	2.29	−97.32	3.6	1.47	−96.96	3.45
16106–5048 <sup>♣</sup>	1.99	−87.55(−92,−80)	5.96	0.95	−87.36(−92,−80)	5.87
16107–4956	0.69	−83.20	2.0	0.32	−82.89	1.45
16148–5011	5.22	−44.76	2.64	4.04	−44.47	2.02
16153–5016	0.58	−41.3	2.5	0.40	−41.44	1.99
16170–5053 <sup>♣</sup>	2.53	−54.2(−59,−49)	4.25	0.55	−53.98	2.78
16187–4932	1.50	−60.58	3.56	0.32	−59.89	1.77
	♣ 0.74	−48.27	2.69	≤ 0.30	—	—
	0.48	−44.65	1.74	≤ 0.30	—	—
16194–4934	1.41	−85.27	3.53	0.56	−84.64	2.67
16204–4916 <sup>♣</sup>	8.34	−70.43(−85,−60)	10.02	4.29	−70.60(−85,−62)	10.35
16204–4943	≤ 0.54	—	—	≤ 0.38	—	—
16218–4931 <sup>♣</sup>	3.33	−37.80(−45,−30)	6.32	2.85	−37.64(−45,−30)	5.1
16219–4848	0.95	−79.99	2.5	0.74	−79.81	2.89
16231–4819	0.42	−59.1	2.4	≤ 0.34	—	—
16232–4917	3.22	−46.41	2.13	2.36	−46.37	1.99
16252–4853	1.19	−45.87	1.72	0.43	−45.77	1.65
16254–4844	1.55	−45.56	3.03	0.56	−45.27	2.44
	♣ 0.93	−40.84	1.49	0.80	−40.85	1.51
16344–4605	♣ 5.93	−61.53	5.25	0.80	−63.95	2.25
	≤ 0.40	—	—	2.95	−60.64	3.54
16358–4614	≤ 0.36	—	—	≤ 0.36	—	—
16363–4645	2.09	−65.29	3.39	1.64	−65.23	2.49
	0.29	−61.02	2.12	0.90	−61.85	3.11
16369–4810	3.48	−39.09	4.58	1.44	−39.31	3.65
16403–4614 <sup>♣</sup>	0.95	−120.1(−124,−117)	3.62	≤ 0.37	—	—
16404–4518	≤ 0.42	—	—	≤ 0.37	—	—
16417–4445	1.14	−56.06	2.2	0.78	−56.13	2.0
16419–4602	2.22	−37.29	2.68	≤ 0.75*	—	—
16428–4109	0.77	−25.65	1.21	0.50	−25.80	1.02
16464–4359	2.55	−79.09	3.14	1.83	−79.44	2.59
16501–4314	5.63	−118.96	3.10	4.13	−118.79	2.68

Table 4. Continued.

source	CS(2–1)			CS(3–2)		
	$\int T_{\text{MB}} dv$ (K km s <sup>−1</sup> )	$v_{\text{LSR}}$ (km s <sup>−1</sup> )	FWHM (km s <sup>−1</sup> )	$\int T_{\text{MB}} dv$ (K km s <sup>−1</sup> )	$v_{\text{LSR}}$ (km s <sup>−1</sup> )	FWHM (km s <sup>−1</sup> )
16535–4300	♣ 1.38	−122.83	2.0	0.90	−123.06	1.67
	♣ 1.02	−88.16	2.75	0.47	−87.91	3.00
16573–4214	3.44	−23.68	2.49	≤ 1.1*	—	—
16581–4212	≤ 0.32	—	—	≤ 0.35	—	—
17033–4035	3.22	−114.77	1.98	1.35	−114.85	1.44
17036–4033	♣ 1.26	−80.17	3.15	0.64	−80.13	3.4
	1.18	−38.49	3.23	≤ 0.39	—	—
17040–3959♣	2.62	−0.40(−6,6)	4.66	2.24	−0.21(−6,6)	5.50
17082–4114	9.15	−20.18	3.50	≤ 0.75*	—	—
17114–3804	≤ 0.37	—	—	≤ 0.40	—	—
17140–3747	≤ 0.36	—	—	≤ 0.38	—	—
17141–3606	0.73	−3.97	1.6	0.19	−3.74	0.8
17156–3607	1.07	−3.15	2.4	0.68	−3.26	2.4
17211–3537	2.67	−69.58	3.37	2.00	−69.60	4.1
17218–3704	0.82	−20.68	1.6	0.60	−20.99	2.47
17225–3426	♣ 4.97	−3.82	1.91	3.51	−4.00	1.73
	1.30	−0.44	3.16	≤ 0.50	—	—
17230–3531	4.29	−91.89	4.2	3.02	−91.52	3.5
17256–3631	3.29	−12.45	3.13	3.29	−12.83	3.22
	♣ 8.02	−8.69	2.60	7.91	−8.80	2.50
17285–3346	0.71	−16.07	2.61	≤ 0.38	—	—
	♣ 1.84	17.60	3.9	0.76	17.15	2.62
17338–3044	1.35	−8.15	2.5	0.65	−8.04	2.36
17355–3241	♣ 2.62	−3.68	2.21	1.28	−3.82	2.15
	0.42	5.87	1.53	≤ 0.40	—	—
17368–3057	≤ 0.37	—	—	≤ 0.43	—	—
17377–3109	10.57(−8,10)	0.20	8.94	10.85	0.58	8.94
17410–3019	3.54	−22.15	2.16	1.89	−22.05	1.74
17419–3207	≤ 0.41	—	—	≤ 0.43	—	—
17425–3017	2.34	−20.23	2.15	2.20	−20.30	3.1

◇ the typical errors from the fits are:  $\sim 0.01 - 0.07$  K km s<sup>−1</sup> in  $\int T_{\text{MB}} dv$ ,  $\sim 0.01 - 0.1$  km s<sup>−1</sup> in  $v_{\text{LSR}}$ , and  $\sim 0.01 - 0.1$  km s<sup>−1</sup> in FWHM

♣ line parameters derived from moment integrals over the velocity range indicated in Cols. 2 and 5 between brackets

♣ component observed also in the C<sup>17</sup>O (1–0) and/or (2–1) spectrum

\* Not observed in the (3–2) line. The upper limits refer to the (5–4) transition



**Table 5.** C<sup>17</sup>O line parameters(<sup>◇</sup>). Typical rms noise in the spectra is  $\sim 0.05$  and  $\sim 0.06$  K for the (1–0) and (2–1) lines, respectively. N.O. = not observed

source	C <sup>17</sup> O (1–0)					C <sup>17</sup> O (2–1)				
	vel. range (km s <sup>−1</sup> )	$\int T_{\text{MB}} dv$ (K km s <sup>−1</sup> )	$v_{\text{LSR}}$ (km s <sup>−1</sup> )	FWHM (km s <sup>−1</sup> )	$\tau_{10}$	vel. range (km s <sup>−1</sup> )	$\int T_{\text{MB}} dv$ (K km s <sup>−1</sup> )	$v_{\text{LSR}}$ (km s <sup>−1</sup> )	FWHM (km s <sup>−1</sup> )	$\tau_{21}$
08211–4158	5,14	1.08	10.99	1.7	$\ll 1$	8,14	2.71	11.04	1.62	$\ll 1$
08247–4223		$\leq 0.9$	—	—	—	N.O.				
08477–4359	4,11	0.75	8.7	2.24	—	N.O.				
08488–4457	N.O.									
08563–4225	3,10	2.95	7.42	1.62	$\ll 1$	5,11	6.80	7.46	1.89	0.2
09014–4736		$\leq 0.5$	—	—	—	N.O.				
09026–4842	1,7	0.75	4.82	0.88	—	3,8	1.78	5.04	1.66	$\ll 1$
09131–4723	0,7	1.39	4.13	2.17	—	1,7	2.80	4.17	1.59	$\ll 1$
09166–4813	2,9	0.58	6.03	1.81	—	3,9	0.73	6.19	2.8	—
09209–5143	33,41	0.61	37.01	2.00	—		$\leq 0.8$	—	—	—
10088–5730	N.O.									
10095–5843	−9,−1	0.89	−4.35	1.85	—	−7,−2	1.71	−4.29	1.1	1.2
10102–5706		$\leq 0.6$	—	—	—	N.O.				
10123–5727		$\leq 0.4$	—	—	—	N.O.				
10156–5804		$\leq 0.5$	—	—	—	N.O.				
10277–5730		$\leq 0.4$	—	—	—		$\leq 0.6$	—	—	—
10308–6122		$\leq 0.5$	—	—	—	N.O.		—	—	—
10317–5936		$\leq 0.5$	—	—	—	N.O.		—	—	—
10439–5941		$\leq 0.5$	—	—	—	−17,−12	1.56	−14.54	1.7	—
10521–6031		$\leq 0.4$	—	—	—		$\leq 0.6$	—	—	—
10537–5930		$\leq 0.5$	—	—	—	N.O.		—	—	—
10545–6244		$\leq 0.4$	—	—	—		$\leq 0.7$	—	—	—
10548–5929		$\leq 0.5$	—	—	—		$\leq 0.8$	—	—	—
10554–6237	−20,−14	0.7	−17.0	2.1	—	−20,−14	1.62	−16.95	2.1	—
10555–5949	N.O.									
10572–6018		$\leq 0.4$	—	—	—		$\leq 0.6$	—	—	—
10575–5844		$\leq 0.4$	—	—	—		$\leq 0.6$	—	—	—
10591–5934		$\leq 0.5$	—	—	—	N.O.		—	—	—
11265–6158		$\leq 0.5$	—	—	—	N.O.				
11294–6257		$\leq 0.5$	—	—	—	N.O.				
11380–6311		$\leq 0.4$	—	—	—	−14,−8	1.02	−11.43	1.78	—
11396–6202		$\leq 0.5$	—	—	—		N.O.	—	—	—
11404–6215		$\leq 0.4$	—	—	—	36,43	0.80	38.52	2.1	—
11476–6435	N.O.									
12102–6133		$\leq 0.5$	—	—	—	N.O.		—	—	—
12295–6224	−41,−35	1.04	−36.86	1.3	0.2	−40,−35	2.10	−36.79	1.3	0.5
12377–6237		$\leq 0.9$	—	—	—	N.O.		—	—	—
12434–6355	N.O.									
13023–6213	−48,−40	0.95	−43.3	2.7	—	N.O.				
13039–6108	−30,−24	0.40	−26.2	0.87	—	−28,−23	1.20	−26.24	0.93	0.6
13078–6247	N.O.									
13106–6050	−62,−53	2.15	−56.87	2.11	$\ll 1$	−60,−55	3.62	−56.89	1.43	0.4
13333–6234	−16,−8	1.66	−11.7	3.67	$\ll 1$	−16,−7	2.51	−11.73	3.6	$\ll 1$
13384–6152	−55,−47	1.73	−50.48	1.93	$\ll 1$	−53,−47	3.53	−50.27	1.65	0.3
13395–6153	−55,−47	2.18	−50.44	2.60	0.3	−54,−47	5.05	−50.56	2.85	$\ll 1$
13438–6203	−56,−48	0.85	−50.75	3.18	—	−53,−49	0.85	−50.98	1.8	—
13481–6124	−45,−37	2.85	−40.7	2.6	0.3	−44,−37	5.52	−40.74	2.68	—
13558–6159	N.O.									
13560–6133	−62,−55	1.19	−57.65	2.41	—	−61,−56	1.92	−58.26	1.5	—
14000–6104	−63,−55	0.80	−58.9	2.5	—	−63,−55	1.60	−58.2	5.3	—
14131–6126	−38,−33	0.69	−34.82	2.26	—	−38,−33	0.99	−34.34	1.44	—
14166–6118	−45,−37	1.82	−41.23	2.53	$\ll 1$	−43,−38	2.30	−41.24	2.5	$\ll 1$

Table 5. Continued.

source	C <sup>17</sup> O (1–0)					C <sup>17</sup> O (2–1)				
	vel. range (km s <sup>−1</sup> )	$\int T_{\text{MB}} dv$ (K km s <sup>−1</sup> )	$v_{\text{LSR}}$ (km s <sup>−1</sup> )	FWHM (km s <sup>−1</sup> )	$\tau_{10}$	vel. range (km s <sup>−1</sup> )	$\int T_{\text{MB}} dv$ (K km s <sup>−1</sup> )	$v_{\text{LSR}}$ (km s <sup>−1</sup> )	FWHM (km s <sup>−1</sup> )	$\tau_{21}$
14183–6050		≤ 0.4	–	–	–	N.O.				
14198–6115	N.O.									
14201–6044	−54, −47	1.16	−49.58	1.75	–	−52, −46	2.64	−49.68	1.7	≪ 1
14395–5941	−47, −39	0.77	−42.13	2.9	–	−45, −40	1.15	−42.23	0.8	–
14412–5948	N.O.									
14425–6023	−50, −42	1.70	−45.22	2.2	≪ 1	−49, −43	4.00	−45.89	2.32	–
14591–5843		≤ 0.4	–	–	–		≤ 0.6	–	–	–
15038–5828	−72, −65	0.65	−68.09	2.04	–	−70, −65	1.23	−67.4	1.27	–
15072–5855	−45, −39	1.35	−41.64	1.6	–	−45, −39	2.68	−41.8	1.4	–
15100–5903	−55, −48	0.89	−51.17	1.94	–	−54, −49	0.62	−51.26	1.58	–
15178–5641		≤ 0.4	–	–	–		≤ 0.5	–	–	–
15219–5658		≤ 0.4	–	–	–	−20, −12	1.37	−16.0	3.0	–
15239–5538		≤ 0.4	–	–	–		≤ 0.6	–	–	–
15246–5612	−70, −60	2.05	−65.32	2.6	≪ 1	−70, −60	3.48	−65.40	1.9	0.5
15262–5541	−58, −52	0.73	−54.3	1.6	–	−56, −52	0.90	−54.17	1.5	–
15347–5518	−65, −58	1.51	−61.4	2.1	–	−65, −58	2.12	−61.39	1.7	≪ 1
15371–5458		≤ 0.4	–	–	–		≤ 0.6	–	–	–
15470–5419	−68, −57	1.88	−61.8	5.3	–	−68, −57	1.94	−61.3	2.27	0.15
15506–5325	N.O.									
15519–5430	−42, −33	2.57	−36.64	2.52	≪ 1	−40, −33	7.18	−36.71	2.24	≪ 1
15557–5337	−51, −42	4.18	−47.0	4.0	≪ 1	−52, −43	14.96	−46.88	3.53	0.4
15571–5218		≤ 0.4	–	–	–		≤ 0.7	–	–	–
15579–5303	−54, −45	2.29	−49.4	4.0	≪ 1	−54, −45	3.29	−49.12	3.6	≪ 1
15583–5314	−82, −75	1.52	−77.76	1.66	≪ 1	−82, −75	2.88	−77.90	1.73	≪ 1
16061–5048	−56, 49	1.80	−51.78	1.60	≪ 1	−54, −48	2.1	−51.80	1.91	≪ 1
16082–5031	−45, −39	1.88	−40.96	1.62	0.3	−44, −39	2.27	−41.01	1.67	0.3
16093–5015	−47, −40	1.47	−42.97	1.41	≪ 1	−46, −40	2.44	−43.02	1.43	≪ 1
16093–5128	−101, −94	1.42	−96.94	2.14	≪ 1	−99, −93	1.77	−96.87	2.14	≪ 1
16106–5048	−93, −85	1.10	−88.76	2.00	≪ 1	−92, −85	1.37	−89.05	2.17	≪ 1
16107–4956	−85, −79	0.59	−82.9	2.0	–	−85, −79	0.33	−82.7	0.6	–
16148–5011	−49, −41	1.06	−44.9	2.2	–	−48, −41	3.00	−44.84	2.0	0.4
16153–5016		≤ 0.4	–	–	–	−44, −38	1.03	−41.43	1.2	1.2
16170–5053		≤ 0.9	–	–	–		≤ 1.0	–	–	–
16187–4932	−53, −43	1.20	−48.27	1.6	–		≤ 0.7	–	–	–
16194–4934	−93, −82	2.02	−85.1	3.4	1.2	−93, −82	1.44	−84.86	2.77	≪ 1
16204–4916	−74, −66	1.01	−69.9	4.9	–	−74, −65	1.78	−69.3	3.23	–
16204–4943	N.O.									
16218–4931	−45, −33	1.59	−38.2	4.8	0.7	−45, −33	2.34	−37.6	4.03	≪ 1
16219–4848		≤ 0.4	–	–	–	−83, −76	0.75	−79.2	0.9	–
16231–4819		≤ 0.6	–	–	–		≤ 1.0	–	–	–
16232–4917		≤ 0.4	–	–	–	−49, −44	1.97	−46.38	1.63	–
16252–4853	−50, −42	0.83	−45.66	1.78	–	−50, −42	0.77	−45.3	2.07	–
16254–4844	−47, −38	1.77	−40.84	1.6	0.3		2.24	−40.91	1.42	≪ 1
16344–4605	−67, −56	1.68	−62.1	3.8	–	−67, −56	2.34	−61.83	2.8	–
16358–4614		≤ 0.6	–	–	–		≤ 1.0	–	–	–
16363–4645		≤ 0.5	–	–	–	−69, −61	0.87	−65.3	3.0	–
16369–4810	−45, −32	2.70	−38.54	5.0	–	−43, −34	2.27	−38.4	3.35	–
16403–4614	−124, −117	0.72	−120.1	1.7	–	−124, −117	0.60	−120.1	1.34	–
16404–4518		≤ 0.6	–	–	–		≤ 1.0	–	–	–
16417–4445		≤ 0.4	–	–	–	−59, −53	0.70	−56.49	0.66	–
16419–4602	−42, −35	1.57	−37.70	1.91	≪ 1	−41, −34	2.35	−37.32	1.7	≪ 1
16428–4109		≤ 0.5	–	–	–	−27, −24	0.93	−25.7	0.99	≪ 1
16464–4359	−83, −75	1.41	−78.81	2.4	–	−83, −75	2.76	−79.4	2.05	0.7

Table 5. Continued.

source	C <sup>17</sup> O (1–0)					C <sup>17</sup> O (2–1)				
	vel. range (km s <sup>−1</sup> )	$\int T_{\text{MB}} dv$ (K km s <sup>−1</sup> )	$v_{\text{LSR}}$ (km s <sup>−1</sup> )	FWHM (km s <sup>−1</sup> )	$\tau_{10}$	vel. range (km s <sup>−1</sup> )	$\int T_{\text{MB}} dv$ (K km s <sup>−1</sup> )	$v_{\text{LSR}}$ (km s <sup>−1</sup> )	FWHM (km s <sup>−1</sup> )	$\tau_{21}$
16501–4314	−123, −116	1.27	−119.0	2.1	$\ll 1$	−123, −116	2.92	−119.0	2.3	0.3
16535–4300	−128, −121	1.69	−122.5	1.46	0.1	−125, −120	2.1	−122.5	1.05	0.8
	−92, −85	0.68	−88.9	4.04		$\leq 0.9$				
16573–4214	−28, −20	2.24	−23.64	2.15	$\ll 1$	−27, −20	4.3	−23.77	1.91	$\ll 1$
16581–4212	N.O.									
17033–4035	−118, −112	1.66	−114.8	1.59	0.4	−118, −112	2.83	−114.8	1.79	$\ll 1$
17036–4033	−84, −78	0.65	−80.4	2.0	—	−84, −78	1.07	−79.85	1.42	—
17040–3959	−7, 4	1.22	0.02	2.5	$\ll 1$	−5, 3	2.3	−0.42	3.23	—
17082–4114	−25, −15	2.4	−19.91	2.6	0.2	−24, −16	3.11	−20.05	1.7	0.9
17114–3804		$\leq 0.6$	—	—	—		$\leq 0.9$	—	—	—
17140–3747		$\leq 0.5$	—	—	—		$\leq 1.0$	—	—	—
17141–3606	−8, −1	0.90	−4.25	1.8	—	$\leq 1.0$	—	—	—	—
17156–3607	−8, −1	1.1	−3.26	1.42	—	−5, −1	1.24	−3.09	1.2	—
17211–3537	−8, −1	1.09	−69.6	2.2	—		1.20	−69.78	2.0	—
17218–3704	−26, −17	1.15	−20.41	1.3	0.8	−23, −19	1.76	−20.6	1.0	0.6
17225–3426	−7, 0	0.64	−3.42	1.6	—	−7, 0	2.90	−3.6	2.7	$\ll 1$
17230–3531	−96, −88	2.68	−91.6	2.8	$\ll 1$	−96, −88	4.12	−91.62	1.57	0.6
17256–3631	−12, −5	0.77	−8.11	1.3	—		2.86	−8.46	1.72	—
17285–3346		$\leq 0.4$	—	—	—	15, 21	1.22	18.05	1.74	—
17338–3044		$\leq 0.5$	—	—	—	−10, −5	0.75	−7.9	1.6	—
17355–3241	−9, 0	1.59	−3.97	1.5	$\ll 1$	−8, −2	1.91	−3.98	1.6	$\ll 1$
17368–3057		$\leq 0.6$	—	—	—		$\leq 0.9$	—	—	—
17377–3109	−5, 8	4.01	2.74	5.7	$\ll 1$	−5, 10	5.83	1.21	7.1	$\ll 1$
17410–3019	−26, −19	1.63	−22.12	1.8	$\ll 1$	−24, −20	2.92	−22.1	1.23	0.5
17419–3207		$\leq 0.6$	—	—	—		$\leq 1.0$	—	—	—
17425–3017	−24, −17	1.25	−19.93	1.4	—	−22, −18	2.2	−20.1	1.14	0.6

◇ the errors from the fits are:  $\sim 0.02\text{--}0.06$  K km s<sup>−1</sup> in  $\int T_{\text{MB}} dv$ ,  $\sim 0.01\text{--}0.1$  km s<sup>−1</sup> in  $v_{\text{LSR}}$ , and  $\sim 0.01\text{--}0.1$  km s<sup>−1</sup> in FWHM

**Table 6.** “Distance-independent” parameters of the clumps. The angular diameters,  $\theta$ , and integrated flux densities,  $F_\nu$ , have been derived from the 1.2 mm continuum maps; the rotation temperatures,  $T_{\text{rot}}$ , the  $\text{C}^{17}\text{O}$  column densities,  $N_{\text{C}^{17}\text{O}}$ , and the  $\text{H}_2$  total column densities,  $N_{\text{H}_2}$ , have been derived from  $\text{C}^{17}\text{O}$  line ratios (assuming a  $\text{C}^{17}\text{O}$  mean abundance of  $3.9 \times 10^{-8}$ ); the  $\text{H}_2$  volume densities,  $n_{\text{H}_2}$ , have been obtained from CS line ratios.

source	$\theta$ ( $''$ )	$F_\nu$ (Jy)	$T_k$ (K)	$N_{\text{C}^{17}\text{O}}$ ( $\times 10^{15} \text{cm}^{-2}$ )	$N_{\text{H}_2}$ ( $\text{cm}^{-2}$ )	$n_{\text{H}_2}$ ( $\text{cm}^{-3}$ )
08211–4158	34.3	2.26	12	2.3	$5.9 \times 10^{22}$	$1.2 \times 10^5$
08563–4225	29.5	4.09	10	7.6	$1.9 \times 10^{23}$	$1.7 \times 10^5$
09014–4736	42.1	0.79				
09026–4842	65.8	1.25	15	1.0	$2.5 \times 10^{22}$	$6.3 \times 10^5$
09131–4723	71.6	4.5	14	1.7	$4.3 \times 10^{22}$	$4.2 \times 10^5$
09166–4813			11	0.4	$1.110 \times 10^{22}$	
09209–5143	64.5	1.43				
10095–5843	33.9	1.16	9	1.8	$4.7 \times 10^{22}$	$1.5 \times 10^5$
10123–5727	43.2	2.41				$1.7 \times 10^5$
10277–5730	27.0	0.63				$4.9 \times 10^4$
10308–6122	33.8	0.45				$2.1 \times 10^5$
10439–5941	42.8	6.90				
10521–6031	6.5	0.46				
10548–5929	65.5	0.62				$5.2 \times 10^4$
10554–6237	21.5	0.73	8	2.9	$7.4 \times 10^{22}$	$4.0 \times 10^4$
10572–6018	37.5	1.31				$4.2 \times 10^4$
11265–6158	30.3	0.50				$2.1 \times 10^5$
11294–6257	17.9	0.27				
11380–6311	51.1	2.53				$1.8 \times 10^5$
11404–6215	9.5	0.70				
12295–6224	45.9	2.4	11	1.6	$4.2 \times 10^{22}$	$1.4 \times 10^5$
12377–6237	15.1	0.53				
13023–6213	28.5	1.39				
13039–6108	50.9	1.38	18	0.7	$1.9 \times 10^{22}$	$1.7 \times 10^5$
13106–6050	33.5	1.95	8	4.5	$1.1 \times 10^{23}$	$5.7 \times 10^4$
13333–6234	31.8	1.5	8	3.7	$9.4 \times 10^{22}$	$2.2 \times 10^5$
13384–6152	30.0	0.45	9	4.2	$1.1 \times 10^{23}$	
13395–6153	24.5	4.2	10	6.8	$1.7 \times 10^{23}$	$8.9 \times 10^4$
13438–6203	33.4	3.9	6	1.8	$4.7 \times 10^{22}$	
13481–6124	25.5	7.12	18	2.8	$7.1 \times 10^{22}$	$1.2 \times 10^5$
13560–6133	18.5	3.1	7	6.0	$1.6 \times 10^{23}$	$1.5 \times 10^5$
14000–6104	50.5	4.4	11	1.3	$3.3 \times 10^{22}$	$4.2 \times 10^5$
14131–6126	$\ll 21$ (#)	0.27	6	43.0	$1.1 \times 10^{24}$	$1.7 \times 10^5$
14166–6118	48.9	1.06	8	2.4	$6.1 \times 10^{22}$	$7.1 \times 10^4$
14183–6050	38.4	0.35				$1.7 \times 10^5$

Table 6. Continued.

source	$\theta$ ( $''$ )	$F_\nu$ (Jy)	$T_{\text{rot}}$ (K)	$N_{\text{C}^{17}\text{O}}$ ( $\times 10^{15} \text{ cm}^{-2}$ )	$N_{\text{H}_2}$ ( $\text{cm}^{-2}$ )	$n_{\text{H}_2}$ ( $\text{cm}^{-3}$ )
14201–6044			23	1.3	$3.4 \times 10^{22}$	
14395–5941	$\ll 21$ (#)	0.46	6	46.1	$1.2 \times 10^{24}$	$2.8 \times 10^4$
14425–6023	20.7	1.46	8	7.4	$1.9 \times 10^{23}$	
15038–5828			17	0.6	$1.6 \times 10^{22}$	
15072–5855	23.6	1.02	8	4.8	$1.2 \times 10^{23}$	$1.2 \times 10^5$
15100–5903	28.	0.95	5	2.4	$6.2 \times 10^{22}$	$2.8 \times 10^4$
15219–5658	15.2	0.52				$5.3 \times 10^4$
15246–5612	20.2	1.26	7	8.4	$2.2 \times 10^{23}$	$4.5 \times 10^4$
15262–5541	46.9	1.82	10	0.5	$1.3 \times 10^{22}$	
15347–5518	48.4	3.12	8	2.1	$5.3 \times 10^{22}$	$2.2 \times 10^5$
15371–5458	43.3	0.67				$3.5 \times 10^5$
15470–5419	39.5	2.41	7	3.1	$8.0 \times 10^{22}$	$2.0 \times 10^5$
15519–5430	32.1	6.38	12	6.4	$1.6 \times 10^{23}$	$2.8 \times 10^5$
15557–5337	38.9	16.7	18	10.3	$2.6 \times 10^{23}$	$3.7 \times 10^4$
15579–5303	21.3	6.26	6	9.2	$2.4 \times 10^{23}$	
15583–5314	39.3	0.53	10	2.7	$6.9 \times 10^{22}$	$1.3 \times 10^5$
16061–5048	27.7	1.64	6	4.8	$1.2 \times 10^{23}$	
16082–5031	35.1	0.54	7	3.6	$9.2 \times 10^{22}$	
16093–5015	34.8	1.81	8	2.9	$7.5 \times 10^{22}$	$8.4 \times 10^4$
16093–5128	43.0	1.28	8	2.1	$5.5 \times 10^{22}$	
16106–5048			11	0.8	$2.0 \times 10^{22}$	
16107–4956			6	0.4	$1.1 \times 10^{22}$	
16148–5011	12.4	2.32	8	11.6	$3.0 \times 10^{23}$	
16187–4932	35.2	0.66				
16194–4934			7	1.3	$3.3 \times 10^{22}$	
16204–4916	32.0	1.37	8	2.2	$5.7 \times 10^{22}$	$2.4 \times 10^4$
16218–4931	16.4	0.69	6	10.1	$2.6 \times 10^{23}$	$2.6 \times 10^4$
16232–4917	16.6	0.45				$4.5 \times 10^4$
16252–4853	43.1	1.22	6	1.2	$3.2 \times 10^{22}$	$2.4 \times 10^4$
16254–4844			12	1.1	$2.9 \times 10^{22}$	
16344–4605	26.6	2.85	7	4.7	$1.2 \times 10^{23}$	
16363–4645	13.0	0.22				$5.7 \times 10^4$
16369–4810			8	1.8	$4.7 \times 10^{22}$	
16403–4614			8	0.5	$1.3 \times 10^{22}$	
16419–4602	17.	2.27	9	2.1	$5.3 \times 10^{22}$	
16464–4359	42.	1.4	10	2.3	$5.9 \times 10^{22}$	$7.1 \times 10^4$
16501–4314	70.9	2.15	15	1.7	$4.3 \times 10^{22}$	$1.0 \times 10^5$
16535–4300	42.0	0.87	8	2.5	$6.5 \times 10^{22}$	$3.5 \times 10^4$
17033–4035			15	1.5	$3.7 \times 10^{22}$	

**Table 6.** Continued.

source	$\theta$ ( $''$ )	$F_\nu$ (Jy)	$T_{\text{rot}}$ (K)	$N_{\text{C}^{17}\text{O}}$ ( $\times 10^{15} \text{cm}^{-2}$ )	$N_{\text{H}_2}$ ( $\text{cm}^{-2}$ )	$n_{\text{H}_2}$ ( $\text{cm}^{-3}$ )
17036–4033			10	0.7	$1.9 \times 10^{22}$	
17040–3959	15.6	0.95	7	8.5	$2.2 \times 10^{23}$	$2.4 \times 10^4$
17082–4114	50.	7.13	8	3.1	$7.9 \times 10^{22}$	
17156–3607			10	0.8	$2.0 \times 10^{22}$	
17211–3537	36.8	1.1	7	1.6	$4.2 \times 10^{22}$	$5.5 \times 10^4$
17218–3704	45.4	1.44	9	1.7	$4.3 \times 10^{22}$	$1.7 \times 10^5$
17225–3426			10	1.7	$4.3 \times 10^{22}$	
17230–3531	21.6	1.19	7	10.9	$2.8 \times 10^{23}$	$4.2 \times 10^4$
17256–3631	18.7	5.6	45	2.0	$5.2 \times 10^{22}$	$7.1 \times 10^4$
17285–3346	11.9	0.26				
17338–3044	19.0	0.19				
17355–3241	45.5	0.6	8	2.2	$5.7 \times 10^{22}$	$4.2 \times 10^4$
17377–3109	17.5	2.0	6	22.7	$5.812 \times 10^{23}$	$1.1 \times 10^5$
17410–3019	18.7	0.16	7	8.2	$2.1 \times 10^{23}$	
17425–3017	21.1	1.59	7	5.1	$1.3 \times 10^{23}$	$2.7 \times 10^4$

# unresolved sources

**Table 7.** Distance ( $d$ ), linear size ( $D$ ), luminosity ( $L$ ), and dust temperature ( $T_d$ ) of all sources detected in CS. A “—” in the columns of  $D$  and  $T_d$  indicates that we could not derive any source angular diameter.

source	$d$ (kpc)		$D$ (pc)		$L$ ( $\times 10^3 L_\odot$ )		$T_d$ (K)
	near	far	near	far	near	far	
08211–4158		1.72		0.29		3.01	28
08247–4223		1.40		—		1.52	—
08477–4359		1.78		—		3.33	—
08563–4225		1.65		0.24		3.16	32
09014–4736		1.32		0.27		3.55	37
09026–4842		1.85		0.59		2.25	26
09131–4723		1.66		0.58		2.61	23
09166–4813		2.25		—		2.11	—
09209–5143		6.38		2.0		13.61	24
10095–5843	1.06	2.92	0.17	0.48	6.97	52.87	24
10102–5706	0.84	2.9	—	—	0.36	4.30	—
10123–5727	0.91	2.95	0.19	0.62	2.47	26.00	34
10277–5730		5.78		0.76		3.24	33
10308–6122(*)		1.18		0.19		1.45	35
10317–5936		8.88		—		57.48	—
10439–5941		2.60		0.54		40.92	—
10521–6031		8.13		0.26		40.26	29
10537–5930		7.22		—		35.77	—
10545–6244(*)		2.00		—		3.19	—
10548–5929		7.60		0.94		39.42	31
10554–6237		2.96		0.31		3.19	27
10555–5949		6.15		—		16.28	—
10572–6018		7.17		1.30		46.65	27
10591–5934		2.84		—		19.00	—
11265–6158		3.39		0.50		5.07	27
11294–6257		3.47		0.30		6.33	30
11380–6311(*)		1.34		0.33		1.33	24
11396–6202		11.16		—		48.57	—
11404–6215		10.97		0.51		74.78	30
12102–6133		4.04		—		7.45	—
12295–6224		4.35		0.97		8.51	22
12377–6237		10.91		0.79		44.87	28
13023–6213		4.82		0.67		18.25	26
13039–6108(*)		2.44		0.60		2.12	26
13106–6050		4.95		0.80		48.76	33
13333–6234	0.94	9.54	0.15	1.47	2.75	284.1	35
13384–6152		5.33		0.78		11.24	26

**Table 7.** Continued.

source	$d$ (kpc)		$D$ (pc)		$L$ ( $\times 10^3 L_\odot$ )		$T_d$ (K)
	near	far	near	far	near	far	
13395–6153		5.34		0.63		277.2	35
13438–6203		5.39		0.87		30.46	24
13481–6124	3.62	7.31	0.45	0.91	73.15	298.4	36
13560–6133		5.56		0.50		33.44	23
14000–6104		5.63		1.38		89.36	33
14131–6126	2.71	8.86	–	–	5.05	54.04	30
14166–6118	3.25	8.42	0.77	2.00	10.02	67.27	32
14183–6050		3.36		0.63		12.94	37
14201–6044	4.05	7.75	–	–	7.56	27.67	–
14395–5941	3.16	9.18	–	–	5.20	43.90	30
14425–6023	3.43	8.92	0.34	0.90	7.30	49.38	26
14591–5843	2.19	10.68	–	–	3.66	87.14	–
15038–5828	5.00	8.00	–	–	11.3	29.0	–
15072–5855(*)		3.00		0.34		4.97	30
15100–5903(*)		3.65		0.50		11.92	33
15178–5641	2.09	11.37	–	–	5.80	161.8	–
15219–5658	1.23	12.29	0.09	0.91	0.90	89.55	28
15239–5538	3.27	10.43	0.41	1.29	13.49	137.2	28
15246–5612	4.48	9.17	0.44	0.90	37.82	158.5	32
15262–5541		3.72		–		5.50	22
15347–5518	4.16	9.79	0.98	2.30	25.68	142.3	35
15371–5458		–( <sup>†</sup> )		–		–	–
15470–5419	4.12	10.16	0.79	1.95	27.90	169.7	32
15519–5430(*)		2.65		0.41		18.62	30
15557–5337	3.29	11.21	0.62	2.11	345.0	4005.3	40
15571–5218	6.63	8.03	–	–	22.55	33.08	–
15579–5303	3.48	11.12	0.36	1.15	19.89	203.1	30
15583–5314	4.99	9.60	0.95	1.83	12.76	47.23	30
16061–5048	3.61	11.35	0.49	1.53	7.92	78.34	28
16082–5031	3.02	12.0	0.51	2.04	21.34	336.9	37
16093–5015	3.14	11.92	0.53	2.01	7.20	103.8	25
16093–5128	6.05	8.90	1.26	1.86	28.92	62.58	30
16106–5048	5.52	9.51	–	–	13.26	39.36	–
16107–4956	5.21	9.90	–	–	16.24	58.64	–
16148–5011	3.27	11.89	0.20	0.72	44.17	584.0	38
16153–5016	3.07	12.08	–	–	33.14	513.1	–
16170–5053	3.75	11.37	–	–	27.49	252.7	–
16187–4932	4.13	11.15	0.71	1.90	11.68	85.13	31



Table 7. Continued.

source	$d$ (kpc)		$D$ (pc)		$L$ ( $\times 10^3 L_\odot$ )		$T_d$ (K)
	near	far	near	far	near	far	
16194–4934	5.30	9.98	–	–	14.98	53.11	–
16204–4916	4.56	10.76	0.71	1.67	25.04	139.4	30
16218–4931	2.90	12.42	0.23	0.99	4.77	87.53	30
16219–4848	5.06	10.33	–	–	9.11	37.97	–
16231–4819	3.88	11.52	–	–	12.87	113.4	–
16232–4917	3.42	11.94	0.28	0.96	13.08	159.4	34
16252–4853	3.41	12.02	0.71	2.51	17.27	214.6	33
16254–4844	3.40	12.04	–	–	7.90	99.12	–
16344–4605	4.36	11.44	0.56	1.48	11.74	80.83	24
16363–4645	4.51	11.25	–	–	84.79	527.6	42
16369–4810(*)		3.12		–		5.107	–
16403–4614	6.28	9.03	–	–	36.13	74.7	–
16417–4445	4.22	11.77	–	–	14.39	111.9	–
16419–4602	3.15	12.74	0.78	3.15	17.90	292.8	30
16428–4109(*)		2.67	–	–		3.97	–
16464–4359	5.27	10.82	1.07	2.20	21.21	89.41	25
16501–4314	6.70	9.49	2.30	3.26	102.8	206.2	30
16535–4300	6.84	9.41	1.39	1.92	25.99	49.19	25
16573–4214	2.60	13.73	–	–	21.98	613.0	–
17033–4035	6.69	9.79	–	–	62.26	133.3	–
17036–4033	5.70	10.79	–	–	25.15	90.12	–
17040–3959(*)		16.48		1.25		988.0	23
17082–4114(*)		2.51		0.62		8.57	24
17141–3606(*)		0.90		–		0.75	–
17156–3607(*)		0.74		–		0.92	–
17211–3537	6.23	10.61	1.11	1.89	32.90	95.42	30
17218–3704(*)		3.32		0.73		16.63	33
17225–3426	1.1	15.77	–	–	14.05	2887.0	–
17230–3531		–(†)		–		–	–
17256–3631(*)		1.96		0.18		63.77	40
17285–3346	3.74	13.17	0.22	0.76	5.86	72.71	30
17338–3044	3.99	13.00	0.37	1.20	9.24	98.08	30
17355–3241(*)		1.71		0.38		2.30	31
17377–3109	0.84	16.15	0.07	1.37	1.51	558.2	31
17410–3019		–(†)		–		–	38
17425–3017		–(†)		–		–	25

(\*) resolved distance ambiguity

(†) no distance estimate

**Table 8.** Clumps masses estimated from 1.2 mm continuum ( $M_{\text{cont}}$ ), assuming virial equilibrium ( $M_{\text{vir}}$ ), from  $\text{C}^{17}\text{O}$  ( $M_{\text{C}^{17}\text{O}}$ ) and from CS ( $M_{\text{CS}}$ ). All values are in  $M_{\odot}$  units.

source	$M_{\text{cont}}$		$M_{\text{vir}}$		$M_{\text{C}^{17}\text{O}}$		$M_{\text{CS}}$	
	near	far	near	far	near	far	near	far
08211–4158		420		93		37		66
08563–4225		596		354		84		55
09014–4736		62		127		–		–
09026–4842		294		208		69		497
09131–4723		993		357		110		190
09209–5143		4419		735		–		–
10095–5843	99	1046	105	290	11	83	18	394
10123–5727	100	1044	161	523	–	–	26	917
10277–5730		1087		497		–		495
10308–6122		30		109		–		34
10439–5941		2697		332		–		362
10521–6031		1831		142		–		–
10548–5929		1991		719		–		993
10554–6237		420		154		55		27
10572–6018		4422		925		–		2144
11265–6158		377		201		–		152
11294–6257		188		126		–		–
11380–6311		345		256		–		148
11404–6215		4871		447		–		–
12295–6224		3847		496		304		913
13023–6213		2220		556		–		692
13039–6108		565		183		53		86
13106–6050		2467		474		577		666
13333–6234	64	6581	314	3183	15	1575	17	1634
13384–6152		879		538		511		372
13395–6153		5773		977		547		514
13438–6203		8602		2652		278		–
13481–6124	4353	17748	460	929	410	4400	248	2050
13560–6133		7674		859		300		417
14000–6104		7202		2676		484		2565
14131–6126	115	1226	–	–	37	399	–	–
14166–6118	600	4024	709	1836	281	1888	743	13010
14183–6050		179		79		–		97
14395–5941	266	2241	–	–	54	457	–	–
14425–6023	1181	7988	354	921	176	1189	63	1174
15072–5855		531		173		113		107
15100–5903		654		297		118		162
15219–5658	49	4934	152	1521	–	–	–	–
15246–5612	1354	5674	431	883	323	1352	88	750
15262–5541		2134		350		–		–
15347–5518	2603	14414	947	2229	395	2186	484	6257
15470–5419	2191	13322	1989	4905	387	2356	227	3411
15519–5430		2591		357		218		448
15557–5337	7468	86702	1155	3934	791	9179	205	8085
15579–5303	4383	44758	1956	6250	238	2427	–	–
15583–5314	763	2824	594	1143	486	1797	529	3784
16061–5048	1343	13273	422	1327	224	2215	216	6590
16082–5031	223	3514	288	1144	189	2982	152	950
16093–5015	1288	18559	232	879	163	2349	143	7815
16093–5128	2709	5862	1716	2525	679	1470	300	1374
16148–5011	1087	14373	144	523	90	1178	–	–
16187–4932	626	4563	938	2532	–	–	–	–
16204–4916	1647	9171	3434	8104	224	1246	202	2623
16218–4931	336	6154	558	2389	107	1965	74	591
16232–4917	262	3199	131	458	–	–	115	910
16252–4853	733	9103	221	780	125	1553	202	8907
16344–4605	4113	28316	1627	4269	299	2061	–	–
16363–4645	175	1088	337	1681	–	–	–	–